**Yutong Xia**
Department of Mechanical Engineering,
University of Michigan,
Ann Arbor, MI 48105
e-mail: yutoxia@umich.edu

**Narayanan Kidambi**
Department of Mechanical Engineering,
University of Michigan,
Ann Arbor, MI 48105;
Exponent, Inc.,
Farmington Hills, MI 48331

**Evgueni Filipov**
Department of Mechanical Engineering,
University of Michigan,
Ann Arbor, MI 48105;
Department of Civil and Environmental Engineering,
University of Michigan,
Ann Arbor, MI 48105

**K. W. Wang**
Department of Mechanical Engineering,
University of Michigan,
Ann Arbor, MI 48105

# Deployment Dynamics of Miura Origami Sheets

*Origami has great potential for creating deployable structures, however, most studies have focused on their static or kinematic features, while the complex and yet important dynamic behaviors of the origami deployment process have remained largely unexplored. In this research, we construct a dynamic model of a Miura origami sheet that captures the combined panel inertial and flexibility effects, which are otherwise ignored in rigid folding kinematic models but are critical in describing the dynamics of origami deployment. Results show that by considering these effects, the dynamic deployment behavior would substantially deviate from a nominal kinematic unfolding path. Additionally, the pattern geometries influence the effective structural stiffness, and it is shown that subtle changes can result in qualitatively different dynamic deployment behaviors. These differences are due to the multistability of the Miura origami sheet, where the structure may snap between its stable equilibria during the transient deployment process. Lastly, we show that varying the deployment rate can affect the dynamic deployment configuration. These observations are original and these phenomena have not and cannot be derived using traditional approaches. The tools and outcomes developed from this research enable a deeper understanding of the physics behind origami deployment that will pave the way for better designs of origami-based deployable structures, as well as extend our fundamental knowledge and expand our comfort zone beyond current practice.*
[DOI: 10.1115/1.4054109]

*Keywords: origami sheet, deployment dynamics, deployable, Miura origami*

## 1 Introduction

Origami is an ancient paper-folding art that can transform a two-dimensional (2D) sheet into a complex 3D structure. It has emerged as a promising tool for the design of mechanical structures with various functionalities. Because origami principles are scale independent, they can be adopted for the design of systems of various sizes and applications, from large-scale space structures [1,2] and civil architectures [3], to mesoscale origami robots [4], and to microscale devices [5,6]. In addition, since that origami can be compactly folded into small volumes and then unfolded to become large systems, they are especially desirable for deployable structure designs [7] that are easy to store and transport when folded. Folding also allows for easy fabrication of these 3D structures, because the process can start with flat 2-D sheets, which are often readily available. And yet, the folding process can allow for advanced geometries including curved surfaces [8]. Previous work has shown that origami sheets can be deformed into complex shapes [9,10], and if the folding protocol is modified, they can also be refolded into new patterns [11].

Origami-inspired material systems can provide extraordinary mechanical properties [12], such as auxeticity [13], nonlinear and tunable stiffness [14–20], multistability [18,21–24], and geometric reconfiguration. Apart from the static/quasi-static features, recent work has explored the suitability of origami for dynamic applications such as noise control [25,26], impact mitigation [27–30], and vibration isolation [31–34]. Even origami-based structures nominally designed for static operations may be subject to dynamic loads from the environment. Thus, it is important to understand the dynamics of origami to achieve desired performances and mitigate safety concerns.

Many of the characteristics and applications of origami structures stem from its ability to design deployable structures. The origami deployment is inherently a dynamic process, where its dynamic characteristics may affect the accuracy, reliability, and efficiency of the deployment transient process and final configuration. In practice, the compliance and the inertia of the system may cause the deployment to deviate from the behaviors predicted by the traditional origami rigid kinematic unfolding analysis. Thus, it is crucial to understand the deployment dynamics for the design and operation of such deployable origami structures.

Origami sheets have been recognized to be a general and basic building block for origami-based structures. Therefore, it is valuable to understand the basic dynamic characteristics of deploying an origami sheet in space. A recent study has analyzed the reaction forces and torques of an origami flasher [35] as it is dynamically deployed. While informative, this work is limited to a specific application and the system transient and vibratory responses during deployment are not explored. There are also recent efforts to investigate the deployment dynamics of tubular origami elements [36,37]; however, their interests are mainly on the assembled tube structure deployed as a space boom, which is very different from a sheet structure that could be much more flexible and nonlinear. To advance the state of art, the goal of this research is to investigate the transient dynamics and overall behaviors of an origami sheet during deployment and develop comprehensive understanding that would support better designs of such structures. In contrast to previous works, the proposed effort investigates the dynamics of sheet-like origami structures with combined panel flexibility and inertial effects, which have been ignored in traditional Miura origami kinematics and deployment studies.

In this research, we select a Miura origami sheet as our platform. The Miura pattern [38] (Fig. 1(*a*)) is a widely used origami pattern design [39,40] that is rigid-foldable and flat-foldable, meaning that the origami structure can be folded to a flat state without deformation in the panels. A Miura origami sheet (Fig. 1(*b*)) consists of an array of repeating Miura origami units. Various actuation methods [41–45] have been proposed for origami deployment, such as actuation via pneumatic devices, stored strain energy, centrifugal force, and shape-memory materials. To focus on the deployment dynamics rather than the details of actuation, in this investigation we select the simple concept of stored strain energy actuation. That is, we consider the Miura origami

Manuscript received September 7, 2021; final manuscript received February 28, 2022; published online April 1, 2022. Assoc. Editor: Radu Serban.

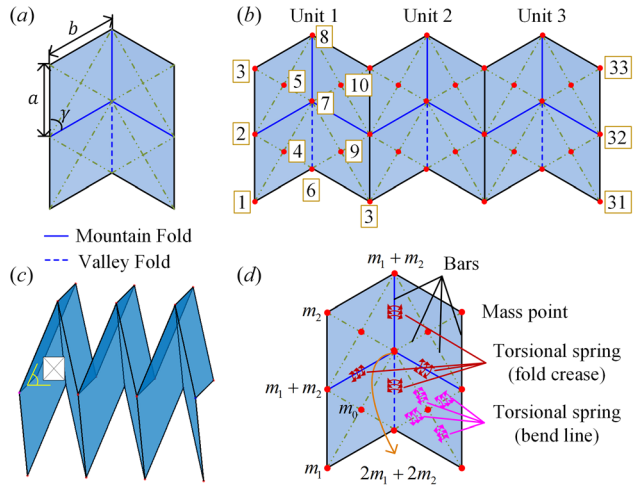


**Fig. 1 (*a*) A Miura origami unit, consisting of four panels connected with fold lines. The dashed line represents a valley fold while the solid lines represent mountain folds. (*b*) A Miura origami sheet consisting of three Miura origami units. Node numbering is denoted in the blocks. (*c*) The folded configuration of the Miura origami sheet with the dihedral angle $\rho$ indicated. (*d*) The bar and hinge model representation for the Miura origami unit. The circular points represent nodes with nonzero mass, which are connected by massless bars (shown as lines). Torsional springs are used for both the fold creases (at both mountain and valley folds), and for the bend lines (within a panel).**

sheet deployment is powered by the strain energy stored in the creases when the sheet is folded. We also assume that a point on the moving boundary condition under deployment is controlled by a given rate. Rather than assuming rigid panels as is common in kinematic origami models, we use a bar and hinge approach [46–49], which allows us to capture deployment behaviors associated with panel deformations and deviate from the traditional pure rigid kinematic analysis. Inertial properties in the model are represented by a system of point masses that reflect the translational and principal rotational inertias of each parallelogram panel in the Miura-origami sheet.

Utilizing numerical analyses, we study the Miura origami system to understand how the dynamic behaviors affect the deployment performance. More specifically, we explore how the panel inertia and elastic deformation cause the dynamic deployment path to differ from the paths predicted by a rigid body kinematic model and a quasi-static model (flexible panels but without considering the inertial effect). We uncover new phenomena that have not been observed previously and cannot be derived via traditional analyses. Some of the system behaviors derived in the analysis are also shown experimentally on a test prototype. Overall, the novel tools and original outcomes developed in this investigation are especially valuable in raising awareness and providing guidelines to create origami with design parameters (e.g., material and geometric properties) and operating conditions (e.g., deployment rate) that are within and outside the traditional range of consideration. In other words, this basic research is impactful in extending our fundamental knowledge and expanding our comfort zone with the deployment dynamics of origami.

In Sec. 2, we introduce a nondimensionalized model that captures the pertinent dynamic behaviors of a Miura origami sheet. Through exploring the influence of structural stiffness and geometric parameters in Secs. 3 and 4, we build a foundation for the design of origami sheets to achieve desired deployment performance. Section 5 discusses how the structural dynamic behaviors change when different deployment control rates are applied, and the role of inertia in the dynamic process. A summary and concluding discussions are presented in the Conclusion section 6.

## 2 Model Formulation

**2.1 Geometry.** A Miura origami sheet is formed by repeating a pattern of mountain and valley creases (Fig. 1(*a*)). A single unit of the Miura origami pattern (Fig. 1(*a*)) is composed of four identical parallelogram panels. It is defined by three independent geometric parameters: two crease lengths $(a, b)$ and the smaller interior angle, also known as the sector angle $\gamma$. Under a rigid folding assumption, all the panels are rigid with no deformation during reconfiguration or folding. With this assumption, the Miura origami theoretically possesses a single degree-of-freedom (DOF). The 3D folded configuration of the whole structure can then be determined by defining one of the dihedral angles inside the Miura origami unit (or sheet). The dihedral angle $\rho$ (shown in Fig. 1(*c*)) is used to describe the sheet's configuration under the rigid folding assumption.

**2.2 Stiffness.** In our research, the panels are not assumed rigid, but with compliance and finite stiffness. The panel stiffness is modeled by a bar and hinge model [46–49], specifically the N5B8 representation where a node is placed in the middle of each panel. By using the N5B8 model, we assume that: (1) the fold creases between panels remain straight even when the adjacent panels deform; and (2) the triangular elements of the panels remain flat while the quadrilateral panels can undergo bending along their diagonals. Each parallelogram panel of the Miura origami sheet is replaced by a N5B8 system as shown in Fig. 1(*d*). The bar and hinge model incorporates material characteristics in its parameters, and reflects a reasonable approximation of scalable, isotropic, and realistic system behaviors, such as in-plane and out-of-plane deformations. For more details about the bar and hinge model, the reader is directed to Refs. [46–49].

The panel in-plane behaviors are represented by bar elements with a stiffness of $k_S = \mathrm{EA}/L$, where $E$ is the Young's Modulus, $L$ is the length of the bar, and $A$ is a representative cross-sectional area of the bar [48] as defined in Eq. (1). The values $A_X$, $A_Y$, $A_D$ refer to the cross-sectional areas of the bars located on the horizontal side, the vertical side, and the diagonal of the parallelogram, respectively. The panel thickness is $t$, the lengths of the two sides of the parallelogram are $H$ and $W$, and $\nu$ is the Poisson's ratio, the values of which are in Table 1. As shown in Eq. (1), changing the panel thickness and the shape of the parallelogram such as the sector angle and side lengths will affect the bar cross-sectional areas and the resulting stretching/shearing stiffness of the panel. The in-plane stiffness of the panels scales linearly with the thickness of the sheet and is orders of magnitude higher than the bending or folding stiffness of the sheet that scale near cubically with the thickness [48]. While the stretching stiffness has been found to be important for more complex origami system such as tubes [50], in this work we found that it does not influence the behaviors of the Miura sheet. Changing the in-plane stiffness results in negligible quantitative, and no noticeable qualitative influence on structural dynamics. Therefore, in the following parametric analyses of the Miura sheet system, the stretching stiffness is kept constant, while other variables are systematically varied

**Table 1 Nominal material and geometric properties of the Miura sheet**

| Parameter | Nominal value |
|---|---|
| Young's modulus $E$ | 70 Gpa |
| Poisson ratio $\nu$ | 0.33 |
| Panel size (side length of the parallelogram) | 0.1 m × 0.1 m |
| Sector angle $\gamma$ | 60 deg |
| Panel thickness $t$ | $10^{-3}$ m |
| Panel density $\rho$ | $3 \times 10^3$ kg/m$^3$ |

$$A_X = t\frac{H^2 - \nu W^2}{2H(1-\nu^2)}$$
$$A_Y = t\frac{W^2 - \nu H^2}{2W(1-\nu^2)} \tag{1}$$
$$A_D = t\frac{\nu(H^2+W^2)^{3/2}}{2HW(1-\nu^2)}$$

As for the out-of-plane stiffness of the panels, Eq. (2) shows the relationship between the bending angle $\theta$ and the reactive torque $M_b$ representing panel bending. We assume a linear region for the moment–rotation relationship, where the stiffness is denoted by $k_b$

$$M_b = \theta \cdot k_b = \theta \cdot \left(0.55 - 0.42\frac{2\gamma}{\pi}\right)\frac{Et^3}{12(1-\nu^2)}\left(\frac{D_S}{t}\right)^{1/3} \tag{2}$$

Equation (2) includes the sector angle $\gamma$, the length of short diagonal $D_S$, the thickness $t$ of the panel, and the material constants Young's modulus $E$, and Poisson's ratio $\nu$. The panel bending stiffness is computed to be $k_b = 406\,\mathrm{N}\cdot\mathrm{m}$ for a Miura panel with nominal material and geometric parameters as stated in Table 1. In our study, the panel bending stiffness $k_b$ and the crease folding stiffness $k_f$ will be used to represent different types of folded origami structures, and to acquire insights into a wider range of origami dynamic behaviors. Here, we introduce a stiffness ratio $r_k \triangleq k_b/k_f$, which is the ratio between panel bending stiffness and crease folding stiffness. This ratio is kept higher than five, which is generally true for most folded origami structures.

**2.3 Inertia.** To represent the inertia of the system in a manner compatible with the bar-and-hinge model, the parallelogram panels in the Miura origami sheet are replaced by sets of lumped masses and the bars and hinges themselves are assumed to be massless. As a result, the Miura origami sheet becomes a simplified finite DOF structure, as shown in Fig. 2(*a*).

We arrange five mass points with prescribed values at the positions of the five nodes in the N5B8 model to represent the inertia of the panel, as shown in Fig. 2(*b*). The values of the mass points are denoted by $m_0$ for the center mass point and $m_1$ and $m_2$ for the mass points at the two different corners of the parallelogram. The mass points along each diagonal share the same value. To capture the inertia properties of the panel, we compute the values of the mass points $(m_0, m_1, m_2)$ that make the first and second moments of inertia of the discretized representation equivalent to those of the continuous panel, as shown in Eq. (3). The value $m_c$ is the mass of the whole panel, $I_c$ is the inertia of the panel, and $I_{mp}$ is the second moment of inertia of the mass point system

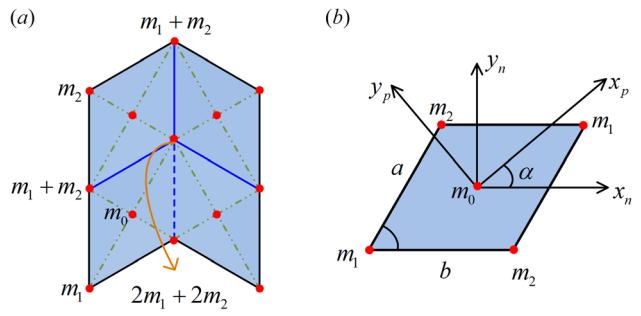


**Fig. 2 (*a*) The lumped mass system that represents the inertia of a Miura origami unit. Mass points are placed at the center and four corners of the parallelogram panels. (*b*) The lumped mass system for each panel, which is a quarter of the Miura origami unit. The vector $x_n$ is the axis parallel to the side *b* of the parallelogram, and $y_n$ is a vector perpendicular to $x_n$. The vectors $x_p$ and $y_p$ are the principal axes of this parallelogram. The angle between these two coordinate systems is $\alpha$.**

$$m_0 + 2m_1 + 2m_2 = m_c$$
$$I_{mp} = I_c \tag{3}$$

The principal moments of inertia $I_{x_p}$ and $I_{y_p}$ of the homogeneous parallelogram panel are derived in Eq. (4). In Fig. 2(*b*), the coordinate systems $x_p$ and $y_p$ are the principal axes of this continuum parallelogram. The angle $\alpha$ is between the principal axis $x_p$ and the axis $x_n$ which is parallel with side $b$ of the parallelogram. The area of the parallelogram is defined as $S$

$$I_{x_p} = \frac{m}{24}\left(a^2 + b^2 - \sqrt{(a^2+b^2)^2 - 4S^2}\right)$$
$$I_{x_p} = \frac{m}{24}\left(a^2 + b^2 + \sqrt{(a^2+b^2)^2 - 4S^2}\right) \tag{4}$$
$$\cos(\alpha) = \sqrt{\frac{a^2+b^2+\sqrt{(a^2+b^2)^2-4S^2} - 2a^2\sin^2(\gamma)}{2\sqrt{(a^2+b^2)^2-4S^2}}}$$

Equation (5) calculates the second moment of inertia of the mass point system in the principal directions of the continuum parallelogram. The position of the $i$th mass point with respect to the origin is defined as $r_i$, and is used to compute the rotational inertia of the node $I_i$.The inertia of the full mass point system $I_{mp}$ is derived by summation of the rotational inertias of all the mass points

$$I_i = m_i(|r_i|^2 - r_i r_i^T)$$
$$I_{mp} = I_0 + I_1 + I_2 + I_3 + I_4 \tag{5}$$

When the values of the mass points are defined as shown in Eq. (6), the first and second moments of inertia of the model match those of the parallelogram plate. Thus, the inertia of a panel can be represented by the set of independent mass points with these designated values

$$m_0 = \frac{2}{3}m_c$$
$$m_1 = m_2 = \frac{1}{12}m_c \tag{6}$$

**2.4 Nondimensional Equations of Motion.** Having established the stiffness and inertia elements of the system, the equations of motion (EOMs) are derived by Lagrange's equations (Eq. (7)). In the bar and hinge model, if no constraints are imposed on the structure, each node will have three degrees-of-freedom

$$\frac{d}{dt}\left(\frac{\partial L}{\partial \dot{x}}\right) - \frac{\partial L}{\partial x} + \frac{\partial D}{\partial \dot{x}} = 0 \tag{7}$$

The Lagrangian is defined by $L(x,\dot{x}) = V(x) - T(x,\dot{x})$, where $V(x)$ is the strain energy of the system, and $T(x,\dot{x})$ is the kinetic energy. The nodal position is defined as $x$, and the nodal velocity is $\dot{x}$.

The total strain energy $V(x)$ consists of contributions from crease folding $V_{\text{fold}}$, panel bending $V_{\text{bend}}$, and panel stretching $V_{\text{stretch}}$. The strain energy from crease folding $V_{\text{fold}}$ results from bending of torsional hinges at the folding creases. The panel bending strain energy $V_{\text{bend}}$ is due to bending of the torsional hinges at bend lines in the model. Finally, the strain energy from stretching in the panels $V_{\text{stretch}}$ is due to elongation and compression of the bars. Strain energy from crease folding or panel bending is computed as in Eq. (8), where $\theta_i$ can be the folding angle $\theta_f$ or the bending angle $\theta_b$, and $M$ is the reactive torque. The force generated on the related node $j$ from the torque $M$ is calculated by Eq. (9). Each dihedral angle $\theta_i$ is formed by its two adjacent triangular panels, containing a total of four nodes; therefore, the partial

derivative $\partial\theta_i/\partial x_j$ results in four vectors. The element $k_{pq}$ in the linearized stiffness matrix resulting from the torque is calculated by Eq. (10)

$$V_i = \sum_i \int_{\theta_0}^{\theta} M(\hat{\theta}_i) d\hat{\theta}_i \quad (i = \text{fold, bend}) \tag{8}$$

$$F_j = \frac{\partial V}{\partial x_j} = \sum_i \frac{\partial V}{\partial \theta_i}\frac{\partial \theta_i}{\partial x_j} = \sum_i M(\theta_i)\frac{\partial \theta_i}{\partial x_j} \quad (i = \text{fold, bend};\ j = 1,2,3,4) \tag{9}$$

$$k_{pq} = \frac{\partial^2 V}{\partial x_p \partial x_q} = \sum_i \left( \frac{\partial M(\theta_i)}{\partial x_p}\frac{\partial \theta_i}{\partial x_q} + M(\theta_i)\frac{\partial^2 \theta_i}{\partial x_p \partial x_q} \right) \quad (i = \text{fold, bend};\ p,q = 1,2,3,4) \tag{10}$$

In the strain energy from panel stretching $V_{\text{stretch}}$, the variable $W$ is the strain energy density function as expressed in Eqs. (12 and 13), in which $E_S$ is the Green–Lagrange strain tensor, with material constants $(\alpha_i, \mu_i, N)$, and axial stretch $\lambda_1$. The corresponding nodal force $F_s$ acting on node $i$ is derived by Eq. (14). The element $k_{pq}$ in the stiffness matrix resulting from stretching deformation is derived by Eq. (15)

$$V_{\text{stretch}} = \sum_{s=\text{bar}} \int_0^{l_s} W(E_S) A_S dx \tag{11}$$

$$W(E_S) = \sum_{i=1}^{N} \frac{\mu_i}{\alpha_i}(\lambda_1{}^{\alpha_i} - 1) \tag{12}$$

$$\lambda_1 = \sqrt{2E_S + 1} \tag{13}$$

$$F_{s,i} = \frac{\partial V_{\text{stretch}}}{\partial x_i} \tag{14}$$

$$k_{pq} = \frac{\partial^2 V_{\text{stretch}}}{\partial x_p \partial x_q} \tag{15}$$

Our dynamic model considers damping due to crease folding and elastic panel deformations, including the panel bending and stretching. The damping from crease folding and panel bending are represented by damping at hinges in the bar-and-hinge model with equivalent damping coefficient $c_f$ (crease folding) and $c_b$ (panel bending), respectively. The nodal force $F_{di}$ of damping from crease folding or panel bending is derived in Eq. (16). The angular velocity $\dot{\theta}$ is a function of the dihedral angle in the hinge $\theta$ and the translational velocity $\dot{x}$: $\dot{\theta} = \frac{d}{dt}\theta(x) = \frac{d\theta}{dx}\frac{dx}{dt}$. The damping from panel stretching is represented by damping of bar deformation in the bar-and-hinge model with damping coefficient $c_{vs}$. The nodal force $F_{ds}$ from panel stretching is shown in Eq. (17), where $l$ is the length of a bar, and $\dot{l}$ is the rate of length change of the bar.

$$F_{di} = c_i \sum_i \dot{\theta}_i \frac{\partial \dot{\theta}}{\partial \dot{x}} \quad (i = \text{fold, bend}) \tag{16}$$

$$F_{ds} = c_{vs} \sum_{j=\text{bar}} \dot{l}_j \frac{\partial l_j}{\partial x} \tag{17}$$

The kinetic energy $T(x, \dot{x})$ is computed by a summation of kinetic energy of each individual node as in Eq. (18). The parameter $m_i$ is the mass of node $i$, and $\dot{x}_i$ is its nodal velocity.

$$T = \frac{1}{2}\sum_i m_i \dot{x}_i^2 \tag{18}$$

We perform nondimensionalization to the EOMs as presented below. The general form of the EOM for a DOF $u_i$ is shown in Eq. (19), in which $u_i$ is the $i$th nondimensionalized nodal displacement. In this equation, the summation over $p =$ fold refers to all the fold creases that are related to this node; the summation over $q =$ bend refers to all bend lines at this node; the summation over $j =$ bar refers to all the bars that are connected to this node. The forces $\bar{F}_{f_p}$ and $\bar{F}_{b_q}$ refer to the nondimensional nodal forces at this node generated by the folding crease $p$ and the bending line $q$, respectively. The force $\bar{F}_{s_j}$ is the nondimensional force from panel stretching deformation of the bar $j$. The nondimensional nodal forces generated from the damping are $\bar{F}_{df_p}$, $\bar{F}_{db_q}$, and $\bar{F}_{ds_j}$ for the folding crease $p$, the bending line $q$, and the bar $j$, respectively. Equations (20)–(25) show detailed expressions for terms in Eq. (19).

$$\bar{m}_i \ddot{u}_i + \sum_{p=\text{fold}} (\bar{F}_{f_p} + \bar{F}_{df_p}) + \sum_{q=\text{bend}} (\bar{F}_{b_q} + \bar{F}_{db_q}) + \sum_{j=\text{bar}} (\bar{F}_{s_j} + \bar{F}_{ds_j}) = 0 \tag{19}$$

$$\bar{F}_{f_p} = \bar{k}_f \bar{L}_p (\theta_p - \theta_{p0}) \frac{\partial \theta_p}{\partial u_i} \tag{20}$$

$$\bar{F}_{b_q} = \bar{r}_k \bar{k}_f \bar{L}_q \theta_q \frac{\partial \theta_q}{\partial u_i} \tag{21}$$

$$\bar{F}_{s_j} = \frac{\bar{L}_j - \bar{L}_{j0}}{\bar{L}_j}\frac{\partial \bar{L}_j}{\partial u_i} \tag{22}$$

$$\bar{F}_{df_p} = 2\xi_0 \bar{c}_f \bar{L}_p \dot{\theta}_p \frac{\partial \theta_p}{\partial u_i} \tag{23}$$

$$\bar{F}_{db_q} = 2\xi_0 \bar{c}_b \bar{L}_q \dot{\theta}_q \frac{\partial \theta_q}{\partial u_i} \tag{24}$$

$$\bar{F}_{ds_j} = 2\xi_0 \bar{L}_j \dot{\bar{L}}_j \frac{\partial \bar{L}_j}{\partial u_i} \tag{25}$$

All the parameters and the variables are nondimensionalized with the parameters found in Table 2. The mass-related variables $(m_0, m_1, m_2)$ are nondimensionalized by $m_0$ which is the mass of the central node in the parallelogram panel. The crease length $a$ depicted in Fig. 1(*a*) is used to nondimensionalize the length-related variables (lengths of folding creases, bending lines, and bar elements). The variable $\tau$ is the nondimensional time, and $\omega_0$ is defined by $\omega_0 = \sqrt{\frac{E A_D}{a\, m_0}}$, in which $A_D$ is the cross-sectional area of the bar along the diagonal of the parallelogram as in Eq. (1). We introduce a parameter $\bar{r}_k$, which is the stiffness ratio between panel bending and crease folding. The damping coefficient of torsional springs is nondimensionalized by the damping coefficient $c_{vs}$ of bar deformation. The damping ratio is defined by $\xi_0 = \frac{a\, c_{vs}}{2 m_0 \omega_0}$.

**Table 2 Nondimensionalization parameters**

| Scales | Non-dimensionalization parameters |
|---|---|
| Mass | $\bar{m} = m_i/m_0, \quad (i = 0,1,2)$ |
| Length | $\bar{L}_i = l_i/a, \quad (i = p,q,s)$ |
| Time | $\tau = \omega_0 t$ |
| Stiffness | $\bar{k}_i = k_i/EA_D, \quad (i = f,b)$ <br> $\bar{r}_k = \bar{k}_b/\bar{k}_f$ |
| Damping | $\bar{c}_i = c_i/a^2 c_{vs}, \quad (i = f,b)$ |

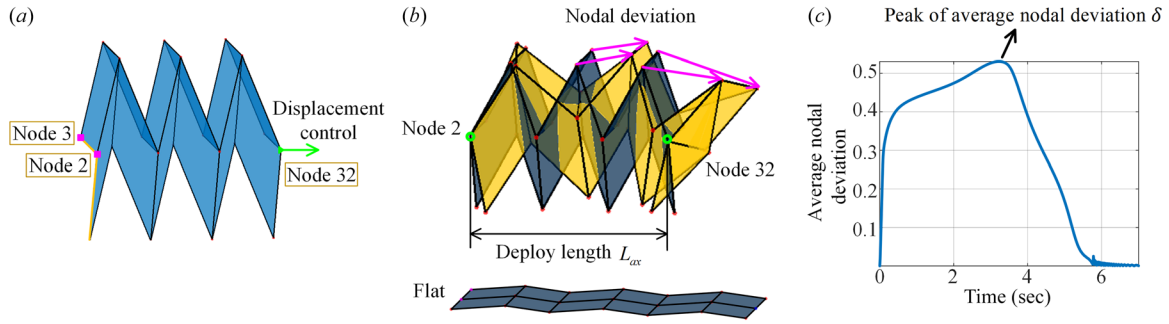


**Fig. 3 (*a*) A Miura origami sheet at a mostly folded stage for illustration of boundary constraints. The nodes with squares on the left end are fixed in all three directions. The node with a triangle on the right end is controlled during deployment and fixed after deployment. The arrow shows the path of displacement control. (*b*) A snapshot during the dynamic deployment with arrows showing deviation between the dynamic configuration (yellow), and the rigid kinematic configuration (blue). (*c*) Time history of the averaged nodal deviation.**

**2.5 Boundary Constraints and Displacement Control.** In this study, the deployment is powered by the strain energy stored in the initially folded stage when the structure is constrained in a small volume. Upon deployment, we fix a few structural nodes on one end of the sheet, control the displacement and rate of a node on the other end, and release all the other constraints. Here, we apply a time-dependent displacement function on a node at the released end of the structure, which mimics a common method where cables or cords are used to control the deployment [47]. We setup three sets of boundary constraints for the Miura origami sheet, one for the initial stowed stage, the second for the deployment process, and the third for the postdeployment stage. These constraints are applied at the relevant nodes, which are numbered according to Fig. 1(*b*). At the initially stowed stage, to ensure compact folding with internally stored energy, we fix all the vertices so that they will remain at the prescribed positions. During the deployment process, to achieve a smooth deployment and avoid additional panel deformation due to boundary constraints, we only fully constrain nodes 2 and 3 at the left end of the Miura origami sheet, denoted by the two squares on the left end in Fig. 3(*a*). Note that if we fixed all three nodes (node 1, 2, 3) on the left end, these nodes would form a V shape (colored in yellow in Fig. 3(*a*)) that remains fixed and prevents full deployment to a flat state. For the right end, we restrain node 32 in the $y$ and $z$ directions and control its position in the $x$ direction, prescribing its motion along a straight path as shown by the green arrow in Fig. 3(*a*). The default rate is 0.6 [−/sec] if not otherwise specified, e.g., in Secs. 3 and 4. In Sec. 5, we discuss the system response under different rates of node 32. In short, we assign different boundary constraints at the three deployment stages: at a folded state and after deployment, all the vertices are fixed in all DOFs; during deployment, nodes 2 and 3 are fixed in all DOFs, and node 32 is fixed in the y and z directions while controlled in the $x$ direction. Under these boundary constraints, the structure will follow the rigid kinematic unfolding path if the panels are assumed rigid. When the structure reaches its fully deployed stage, in which the sheet is flat, the displacement rate control will end and node 32 will be fixed at the final position. In our analysis, the stress-free state is the flat configuration. Before deployment starts, the Miura origami sheet is folded into a compressed state with a fold angle of $\rho = 80$ deg.

## 3 Influence of Structural Material Stiffness on the Dynamic Deployment Process

In this section, we investigate the role of the crease folding stiffness and the ratio between the panel bending stiffness and crease folding stiffness on the structural dynamic response. We perform numerical simulations on the nondimensional model. The structure starts to deploy when the Miura origami sheet is released, and a displacement control with a constant velocity 0.6 [−/sec] is applied to the right end to guide the deployment process (Fig. 3(*a*)). Unlike the single DOF rigid kinematic unfolding process, the panels undergo bending and stretching deformations, and the entire Miura origami sheet shows transient oscillation during the deployment.

In Figs. 3 and 4, we use yellow color to represent the dynamic deployment configuration of the sheet, while blue color refers to the corresponding rigid unfolding configuration at the same stage of deployment. The deployment stage is defined using the distance between the fixed node 2 and the controlled node 32 in the $x$ direction, denoted by $L_{ax}$ in Fig. 3(*b*). We represent the deployment stage using a percentage of the length of the current configuration, $L_{ax}$, with respect to that of the fully deployed flat configuration (Fig. 3(*b*)). To quantitatively evaluate the dynamic behaviors of the Miura origami sheet, we compare the dynamic configuration with the corresponding kinematic configuration at the same deployment stage, and compute the deviation for each of the nodes (four sample node deviations are shown with pink arrows in Fig. 3(*b*)). The average of the magnitude of the deviation among all the nodes is used to evaluate the difference between the dynamic deployment configuration and the rigid kinematic unfolding configuration, which is presented as a function of time in Fig. 3(*c*). To characterize the performance of the deployment process, we employ the peak value of the averaged nodal deviation $\delta$ that occurs during the deployment time history (e.g., 3.8 s in Fig. 3(*c*)) as an index for comparison.

From the normalized stiffness terms in Eq. (20), we vary the effective stiffness by changing the stiffness variables $(\bar{r}_k, \bar{k}_f)$, where the structure may exhibit qualitatively very different deployment behaviors. The deployment processes of three structures with different stiffness ratios $\bar{r}_k$ are shown with snapshots in Fig. 4. In cases where the panel stiffness is similar in magnitude to the fold stiffness, the structure undergoes a large global bending and snaps into a "pop-up" configuration. This pop-up occurs at different stages depending on the stiffness ratio. In Fig. 4, the structure with $\bar{r}_k = 5$ undergoes pop-up earlier during deployment than structure with $\bar{r}_k = 7$. However, as the stiffness ratio $\bar{r}_k$ increases, the dynamic deployment starts to follow closer to the rigid kinematic unfolding, and as with $\bar{r}_k = 10$ and higher, the pop-up does not occur throughout the deployment process. Experimentally, we observe similar behaviors through studying a proof-of-concept prototype as shown in Fig. 5. The facets are built by two layers of paper, and are connected by a thin 0.5 (mm) plastic sheet in the middle (Fig. 5(*i*)). The dimensions are the same as listed in Table 1. The deployment is guided by stored strain energy and a displacement control on the right end denoted by the white arrow. The structure can stabilize at configurations similar

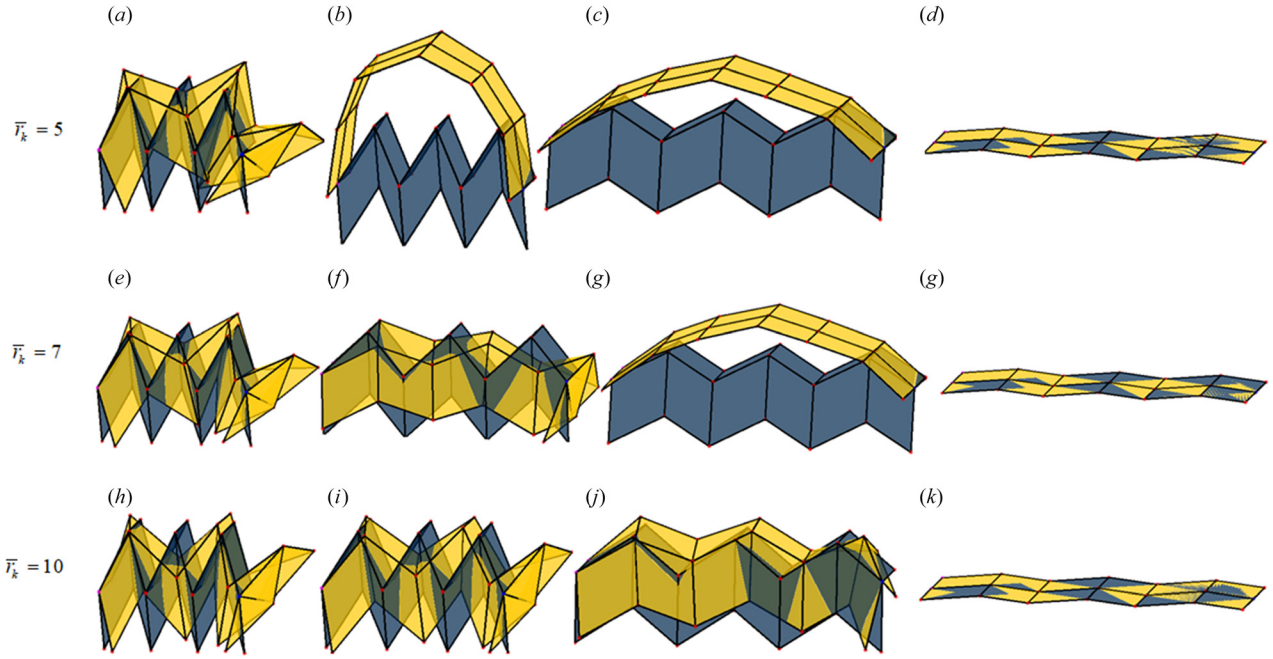


**Fig. 4 Snapshots of the deployment process of the three-unit Miura origami sheet structure with different stiffness ratios: (*a–d*) $\bar{r}_k = 5$; (*e–g*) $\bar{r}_k = 7$; and (*h–k*) $\bar{r}_k = 10$. The fold stiffness is the same for all cases with $\bar{k}_f = 3.8\times10^{-7}(\bar{k}_f/\bar{k}_{f0} = 1)$: (*a*) $t = 0.5$ sec, (*b*) $t = 1.5$ sec, (*c*) $t = 5$ sec, (*d*) $t = 16$ sec, (*e*) $t = 1$ sec, (*f*) $t = 3.5$ sec, (*g*) $t = 5$ sec, (*h*) $t = 0.5$ sec, (*i*) $t = 1.5$ sec, (*j*) $t = 4.5$ sec, and (*k*) $t = 16$ sec.**

to those captured in the snapshots of the dynamic process from the analysis, indicating that the different dynamic configurations are the results of the different stable equilibria of the structure at different deployment stages. In Fig. 5, the model exhibits the squeezed configuration (Fig. 5(*a*)), a pop-up configuration (Figs. 5(*b*), 5(*c*), and 5(*f*)), a less distorted shape at a more deployed stage (Figs. 5(*d*), 5(*g*), and 5(*h*)), and the stress-free flat state (Fig. 5(*e*)).

The global pop-up motion in the snapshots (Fig. 4) results in large nodal deviations and is dependent on stiffness. We perform

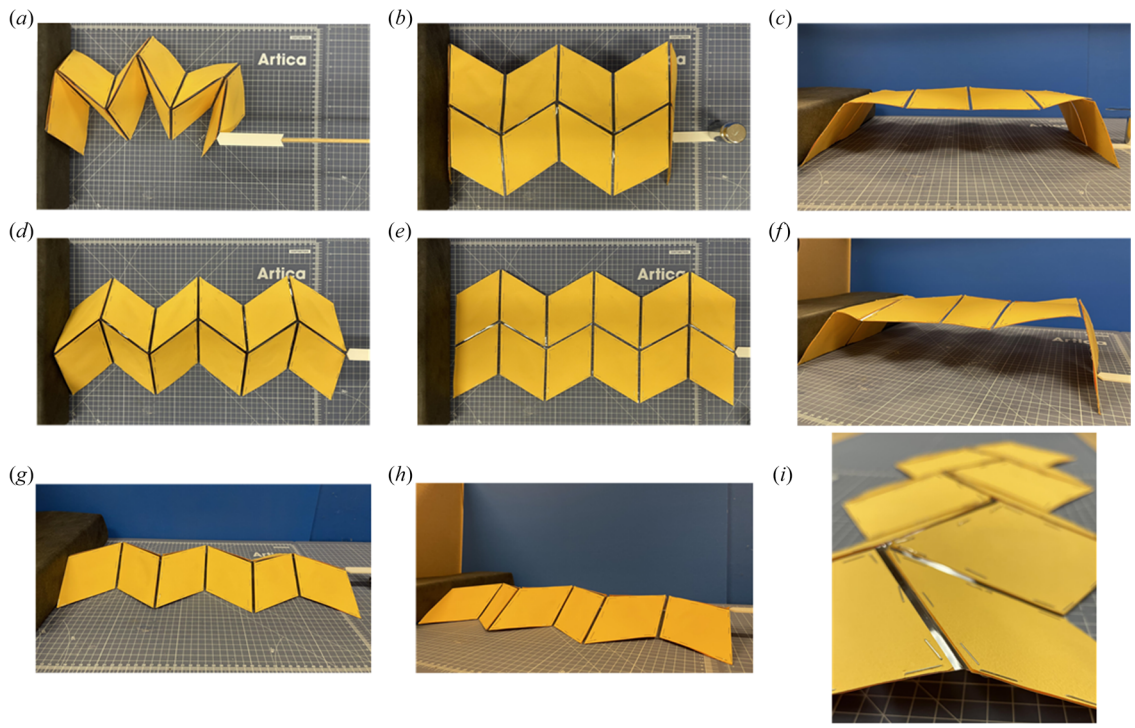


**Fig. 5 Experimental investigation: snapshots of the configurations at different deployment stages of a three-unit Miura origami sheet prototype. The upper crease on the left end is fixed, and the center vertex on the right end is controlled, denoted by the white arrow. (*a*) Refers to a folded state, (*b*) refers to a pop-up state, with (*c*) and (*f*) showing a front view and side view of the pop-up state, respectively. (*d*) Refers to a more deployed state with (*g*) and (*h*) showing a front view and side view. (*e*) Refers to the flat configuration. (*i*) Shows a detailed view of the crease.**

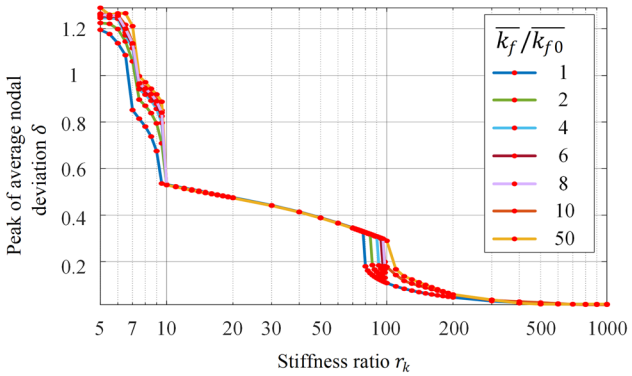


**Fig. 6 A parametric study of the stiffness coefficients for a three-unit Miura origami sheet. We vary the stiffness ratio $\bar{r}_k \in [5, 1000]$, where five refers to a system where panels and folds have a similar stiffness (e.g., a paper prototype), and 1000 refers to a system where the panels are much stiffer (e.g., metal panels connected with hinges). The *x*-axis is the stiffness ratio $\bar{r}_k$ in log scale, and the *y*-axis is the peak value of the averaged nodal deviations $\delta$ on a linear scale. The curves in different shades indicate different fold stiffness $\bar{k}_f$. We vary the $\bar{k}_f$ with respect to $\bar{k}_{f0} = 3.8\times10^{-7}$, and present a normalized ratio. In the regions $\bar{r}_k \in [10, 70]$ and $\bar{r}_k > 200$, the difference between results is small, and the curves overlap each other.**

a parametric study on the stiffness coefficients ($\bar{r}_k$, $\bar{k}_f$) and compute the corresponding $\delta$ for each of the deployment processes (Fig. 6). We use a normalization value $\bar{k}_{f0} = 3.8 \times 10^{-7}$ to allow for simpler representation of the folding stiffness. The structures with higher $\bar{k}_f$, meaning stiffer fold lines, result in slightly higher $\delta$ than those with lower fold stiffness but the same ratio $\bar{r}_k$. Because the deployment is facilitated by strain energy stored in the fold creases, systems with higher $\bar{k}_f$ have more energy stored initially, which results in more reactions among units during the dynamic motion and more panel deformation, and thus higher overall deviation. The stiffness ratio $\bar{r}_k$ has more significant effects on the structural dynamic behaviors. As the ratio $\bar{r}_k$ increases, meaning that the panels become stiffer relative to the folds, there is less panel bending, and the deviation $\delta$ decreases to zero where the structure follows the nominal rigid unfolding path. Three sharp declines are observed in the averaged nodal deviation peak, the first between $\bar{r}_k = 7$ and $\bar{r}_k = 8$, the second between $\bar{r}_k = 9$ and $\bar{r}_k = 10$, and the last between $\bar{r}_k = 78$ and $\bar{r}_k = 100$, depending on the fold stiffness $\bar{k}_f$. These three drops happen due to distinct changes in the structural behaviors. Before the first drop of $\delta$ in Fig. 6, the stiffness of the panels is similar to the stiffness of the folds. The corresponding structure snaps into the "pop-up" state as soon as it is released from the initial boundary constraints (Figs. 4(*a*)–4(*d*)), which results in the highest nodal deviations. As the panel to fold stiffness ratio increases to $\bar{r}_k = 7$, there is a drop in the deviation, because the structure only pops up later during the deployment process (see difference between Figs. 4(*b*) and 4(*f*)). This later occurrence of the pop-up deformation results in a relatively smaller $\delta$ than if the pop-up occurs at the beginning of the deployment process. The second drop in deviation in Fig. 6 occurs when the panels are further stiffened with a ratio of $\bar{r}_k = 10$. In this case, despite some modest deviations, the system remains close to the rigid kinematic unfolding configuration, and no pop-up occurs throughout the deployment process. As the panel to fold stiffness ratio increases beyond $\bar{r}_k = 10$, the origami sheet will not pop up, indicating the existence of a critical value for the stiffness coefficient $\bar{r}_k$, beyond which large global deviations can be avoided. We define the minimum stiffness ratio that keeps the structure from pop-up as $\bar{r}_{km}$. In Sec. 4.2, we will discuss that this critical value $\bar{r}_{km}$ also depends on the number of units in the Miura origami sheet. The nodal deviations undergo the third drop around $\bar{r}_k = 78$ with $\bar{k}_f/\bar{k}_{f0} = 1$, and at successively higher ratios for structures with stiffer folds (up to $\bar{r}_k = 100$ for structures with $\bar{k}_f/\bar{k}_{f0} = 50$). We select the curve with $\bar{k}_f/\bar{k}_{f0} = 1$ for illustration and compare the case $\bar{r}_k = 78$ with $\bar{r}_k = 80$, as shown in Fig. 7. When released, the softer structure ($\bar{r}_k = 78$) snaps into a configuration with uneven deviations among the different units, where the rightmost unit is more compressed, while the left and middle units are more deployed than the rigid unfolding configuration (Fig. 7(*a*)). Later in the deployment process, the structure snaps back to a more uniform configuration that closely follows the rigid configuration, as shown in Fig. 7(*c*). As for the stiffer case ($\bar{r}_k = 80$), the structure always stays at near the rigid unfolding configuration throughout deployment, and the deviations are thus much smaller.

This study shows that the structure can exhibit significantly different behaviors as a function of stiffness. The fold stiffness $\bar{k}_f$ directly affects the initially stored strain energy, and a higher fold stiffness can slightly increase the deviation between systems with the same ratio $\bar{r}_k$. The ratio $\bar{r}_k$ plays a more important role than the absolute value of the fold stiffness. Low $\bar{r}_k$ values result in

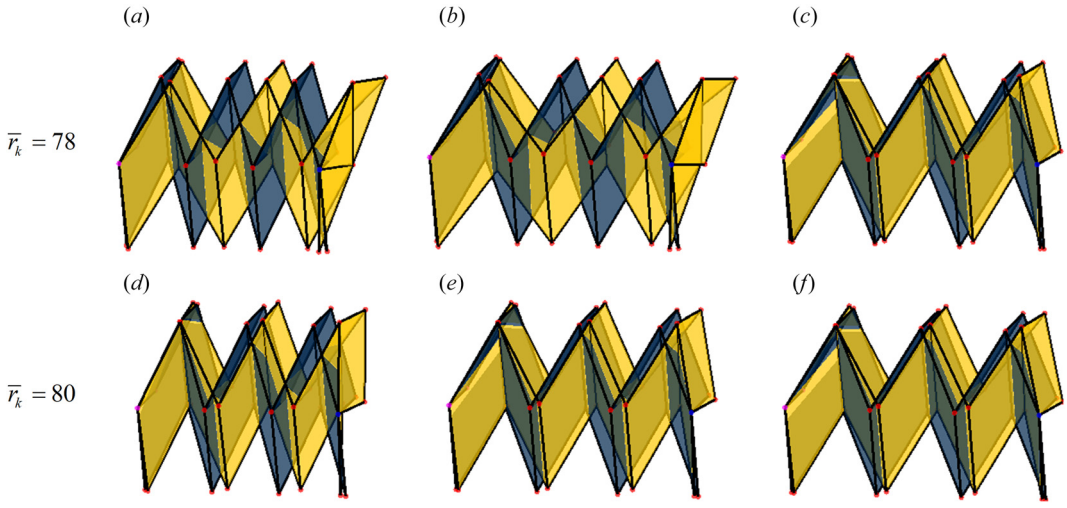


**Fig. 7 Snapshots of the deployment process of structures with (*a–c*) $\bar{r}_k = 78$; and (*d–f*) $\bar{r}_k = 80$. Both structures have $\bar{k}_f/\bar{k}_{f0} = 1$. These two deployment processes correspond to directly before (*a–c*) and after (*d–f*) the third drop in the $\bar{k}_f/\bar{k}_{f0} = 1$ curve in Fig. 6. The two systems have different extents of deviation from the rigid path: (*a*) $t = 0.5$ sec, (*b*) $t = 1.2$ sec, and (*c*) $t = 1.4$ sec.**

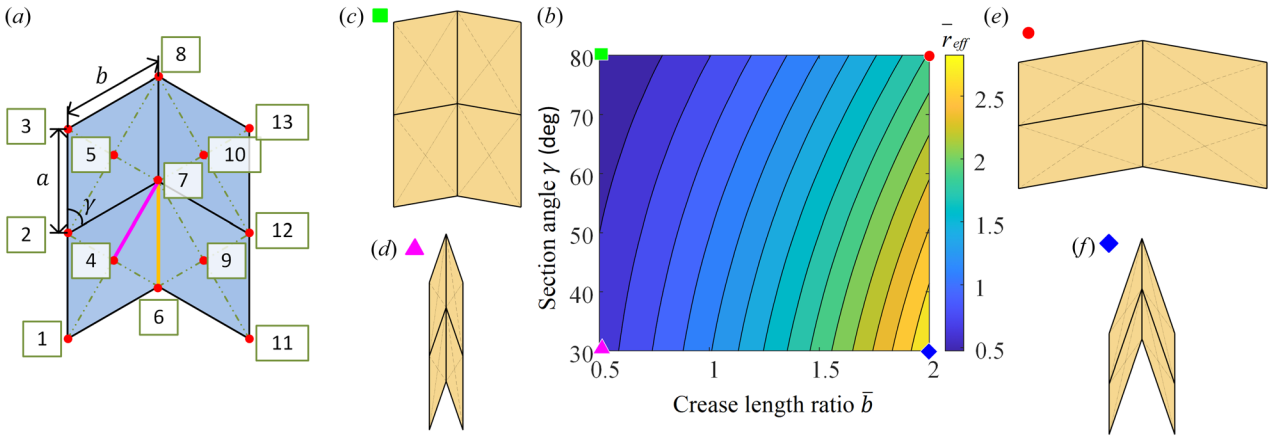


**Fig. 8 (*a*) A unit of the Miura with the fold line (yellow) that is related to the movement of nodes 6-7-4-9, and the bend line (pink) related to nodes 4-7-2-6. (*b*) Contour plot of the effective stiffness ratio $\bar{r}_k$, which is shown in the *z*-direction with shading. The parameter space is spanned by the crease length ratio $\bar{b}$ in the *x*-axis and the sector angle $\gamma$ in the *y*-axis. (*c*–*f*) show the extreme cases of geometric parameters at the four corners of the contour plot.**

large panel deformations and possibly a global pop-up type motion. When the ratio $\bar{r}_k$ is increased beyond a critical value $\bar{r}_{km}$, the pop-up behavior is inhibited, and the structure eventually follows the rigid kinematic unfolding configuration.

## 4 Influence of the Number of Units and Pattern Geometry

According to Sec. 3, the structural dynamic deployment behaviors can be greatly influenced by changing the material stiffness coefficients, especially the stiffness ratio $\bar{r}_k$. Large $\bar{r}_k$ represents stiffer panels compared to the fold lines, and thus less deformation and deviation occurs during the deployment when compared to the rigid unfolding case. In this section, we will show that, other than the material stiffness coefficients, the number of units and geometry of the origami can also change the effective stiffness of the structure (Sec. 4.1), and thus will affect the dynamic deployment process (Secs. 4.2 and 4.3).

**4.1 Influence of Number of Units and Geometry on Structural Stiffness Properties.** The EOM in Eq. (20) reveals that the nodal force can be affected by the crease length $L$ and partial derivative $\partial\theta/\partial u$, which implicitly contain other geometric parameters and thereby affect the overall stiffness of the crease. Here, we first examine one unit to show how the effective stiffness ratio between a fold line and bend line (Fig. 8(*a*)), defined as $\bar{r}_{eff} = \bar{L}_p \frac{\partial\theta_p}{\partial u_i} / \bar{L}_q \frac{\partial\theta_q}{\partial u_j}$, is affected by the geometric parameters. The contour plot in Fig. 8(*b*) shows the effective stiffness ratio with respect to the crease length ratio and the sector angle. The crease length ratio is the ratio between the length of the horizontal folds and the length of the vertical folds: $\bar{b} = b/a$ (Fig. 8(*a*)). A unit with a low sector angle of 30 deg and a high crease length ratio of 2 (Fig. 8(*f*)) has an effective stiffness ratio that is about five times higher than that of the unit with a sector angle of 80 deg and crease length ratio of 0.5 (Fig. 8(*c*)). These large differences in the effective stiffness ratio indicate that the geometric parameters can have a significant effect on the global stiffness properties, and thus may influence the deployment dynamics.

As the origami sheet deploys, its overall geometric shape changes with the folding angle, which will affect the effective stiffness of the system. This shape change occurs even though the base geometric parameters $\gamma$ and $\bar{b}$ are kept constant. Because the mass of the structure remains proportional to the size of the structure, the modal natural frequencies derived from an eigen-analysis can provide a direct representation of the effective structural stiffness. Here, we perform an eigen-analysis on the static equilibrium state of the system at different points along the deployment path. We apply the same boundary constraints as in the dynamic analysis except that we fix node 32 at each stage along the deployment path. The static equilibrium state is obtained by allowing the nodal position of the origami to converge to a new configuration through an iterative process of the static governing equations (delete the time varying variables and inertial and damping terms from the dynamic EOM) which minimizes the sum of internal forces within the system. An eigen-analysis using the mass and stiffness matrices of the structure is then performed to find the natural frequencies and the corresponding fundamental modes. Figure 9 shows results from this analysis for different points along the deployment path of the origami. This three-unit sheet has a crease length ratio at $\bar{b} = 1$, sector angle at $\gamma = 60$ deg, and stiffness parameters ($\bar{r}_k = 100$, $\bar{k}_f/\bar{k}_{f0} = 1$). The natural frequencies of the structure increase with deployment, and reach a peak value followed by a sharp decline near the fully deployed stage (Fig. 9(*g*)). At a low deployment extent of 5%, the first two eigenmodes refer to deployment mainly in the longitudinal direction (Figs. 9(*b*) and 9(*c*)), while the third eigenmode refers to a near pop-up transverse or bending configuration (Fig. 9(*a*)). As the deployment increases to 20%, the second (Fig. 9(*e*))) and third (Fig. 9(*d*)) eigenmodes switch in order. As the structure becomes more deployed, the eigenmodes become significantly different (Figs. 9(*h*)–9(*j*)). A sharp reduction in the natural frequencies is observed around the deployment extent of 100%. By comparing the shape of the eigenmodes at 99% and 100%, we see that the behavior changes drastically, and the origami sheet at a flat state has modes that resemble the transverse bending modes of an elastic beam (Figs. 9(*l*)–9(*m*)). In these modes, the deformation concentrates at the creases, which results in less energy and a lower natural frequency.

To obtain a more comprehensive understanding, these eigenvalue analyses are performed for the sheet with different geometric parameters and with different numbers of units. Figure 10 shows contour plots of the first mode natural frequency $\omega_n$ for structures with different parameters (crease length ratio $\bar{b}$, sector angle $\gamma$, and number of units) presented in the horizontal axis and the deployment stage in the vertical axis. Structures with higher $\bar{b}$ appear softer (lower natural frequency) given the same stage of deployment (Fig. 10(*a*)). From Fig. 10(*b*), we see that the maximum natural frequency (and stiffness) occurs for structures with a sector angle $\gamma$ of around 60 deg. For low deployment stages, structures with $\gamma < 57$deg, have a discontinuity in the natural frequency values which is due to the stable quasi-static state entering another equilibrium state as will be discussed in Sec. 4.3.3. In Fig. 10(*c*), we perform the eigenvalue analysis on sheets with

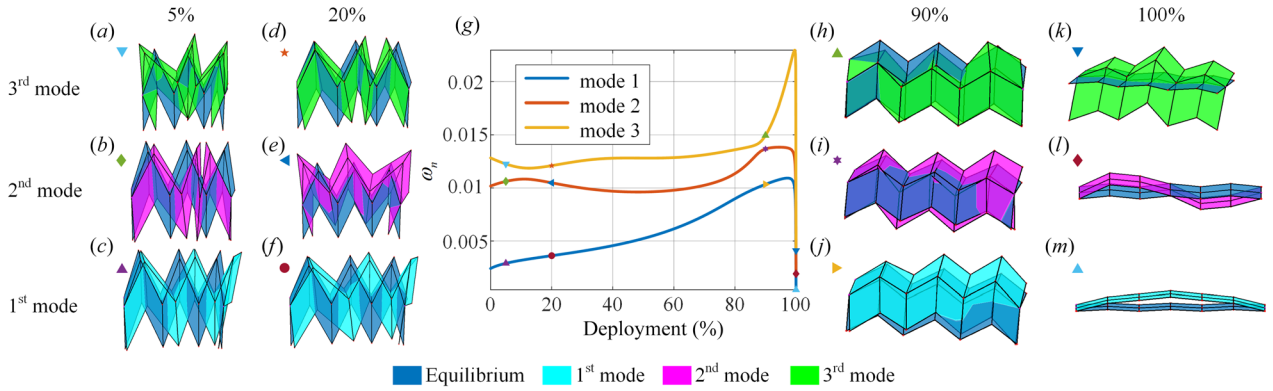


**Fig. 9 The first three natural eigenmodes of the sheet. (*g*) The natural frequencies as a function of the deployment stage. In the snapshots, the darkest configurations refer to the quasi-static equilibrium position, and the remaining shades (cyan, magenta, and green in clolored version of this figure) refer to the shape of the first three eigenmodes. Each row corresponds to a certain mode, while each column corresponds to a certain extent of deployment.**

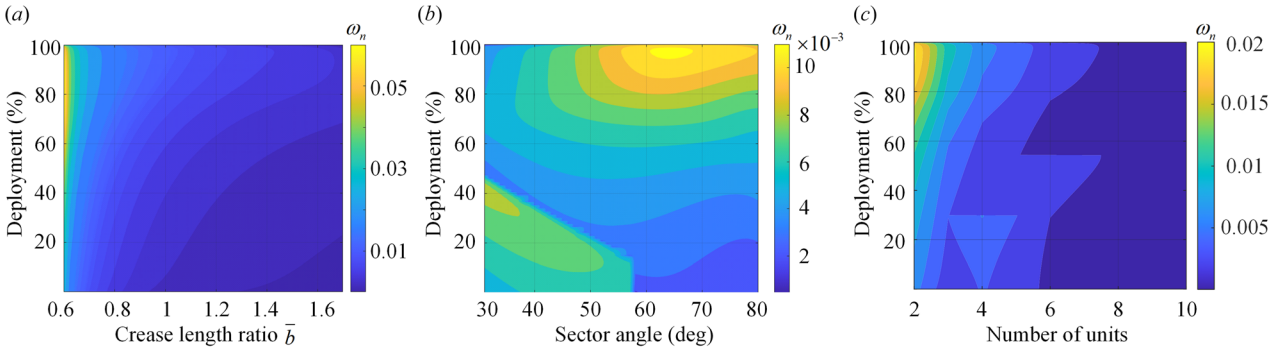


**Fig. 10 The first mode natural frequency $\omega_n$ of the Miura sheet structure with different geometric parameters. The geometric parameter is varied with the *x*-axis and the deployment stage with the *y*-axis. (*a*) Different crease length ratios $\bar{b}$, where the sector angle is kept at $\gamma = 60deg$, and there are three units in the sheet. (*b*) Different sector angles, where the crease length ratio is kept at $\bar{b} = 1$, and there are three units in the sheet. (*c*) A different number of units in the sheet, while the crease length ratio is kept at $\bar{b} = 1$, and the sector angle is kept at $\gamma = 60$ deg. (Note: a continuous contour is presented, but only discrete values of the number of units are used in *c*).**

different numbers of units and show that the Miura origami sheets consisting of more units tend to be softer (lower natural frequency) because more creases and panels in the structure allow for more global deformation. Note that with more units, the internal mass and stiffness of the structure both increase proportionally, but the overall effective stiffness decreases. The apparent discontinuities in Fig. 10(*c*) occur because the contour lines have fixed values, and there is sparse data in the horizontal direction corresponding to discrete values for the number of units. With all different parameter variations, as the structures become more deployed (i.e., around 80–99%), they exhibit a higher natural frequency and effective stiffness similar to the results observed in Fig. 9(*g*).

**4.2 Influence of Number of Units on the Dynamic Deployment Process.** The eigen analysis in Sec. 4.1 showed that origami sheets consisting of more units have a lower natural frequency and lower effective stiffness (Fig. 10(*c*)). In this section, we investigate the dynamic deployment behavior of origami sheets with different numbers of units. Figure 11 shows that the nodal deviation $\delta$ increases with the number of units, indicating that the longer and more flexible structures experience more deformation as can be expected.

The value of the critical stiffness ratio $\bar{r}_{km}$ at which the structure will no longer experience a pop-up deformation (Figs. 4(*b*), 4(*c*), and 4(*g*)) also varies with the number of units in the structure. We vary the number of units and perform dynamic analyses on structure with different stiffness parameters ($\bar{r}_k$, $\bar{k}_f/\bar{k}_{f0}$), and show the relationship between the nodal deviation $\delta$ and stiffness parameters ($\bar{r}_k$, $\bar{k}_f/\bar{k}_{f0}$) for systems with 5, 7, and 10 units (Figs. 12(*a*)–12(*c*)). As discussed in Sec. 3, the ratio $\gamma$ plays a more significant role than the fold stiffness in affecting the qualitative deployment behavior. For stiffness ratios lower than $\bar{r}_{km}$, the structure undergoes a pop-up and results in high nodal deviation, while for higher stiffness ratios, the pop-up is avoided, and the

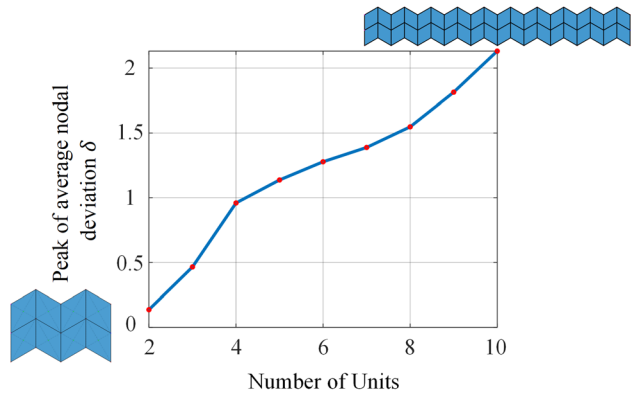


**Fig. 11 Nodal deviation $\delta$ increases with the number of units in the origami sheet. The Miura sheet has the geometry of ($\bar{b} = 1$, $\gamma = 60$ deg), and stiffness parameters of ($\bar{r}_k = 100$, $\bar{k}_f/\bar{k}_{f0} = 1$). With these stiffness parameters, the structures do not experience the pop-up deformation observed earlier in Sec. 3.**

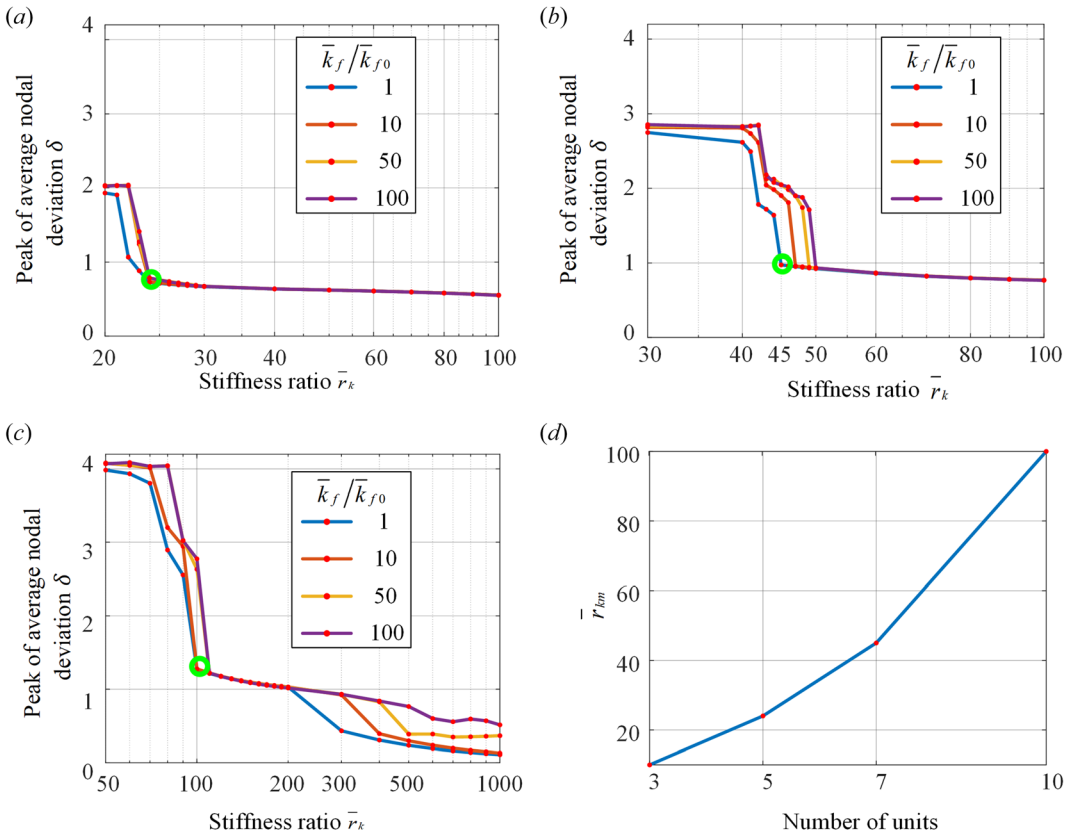


**Fig. 12 Stiffness ratio with respect to the nodal deviation for (*a*) a five-unit, (*b*) a seven-unit, and (*c*) a 10-unit Miura origami sheet. In (*a–c*), the $\bar{r}_{km}$ is circled for the case where $\bar{k}_f/\bar{k}_{f0} = 1$. (*d*) The critical value $\bar{r}_{km}$ for $\bar{k}_f/\bar{k}_{f0} = 1$, which is the minimum stiffness ratio to avoid a "pop-up" deformation, is higher as more units are used in the Miura origami sheet.**

structure follows the rigid kinematic configuration more closely. The analyses on structures with 5, 7, and 10 units show the same qualitative behaviors (Figs. 12(*a*)–12(*c*)). Moreover, the critical ratio $\bar{r}_{km}$ increases as we increase the number of units, and a higher stiffness ratio $\bar{r}_k$ is needed to avoid pop-up in the longer and more flexible structures (Fig. 12(*d*)). In other words, stiffer panels are needed to avoid the pop-up deformation for longer sheets.

**4.3 Influence of Geometry on the Dynamic Deployment Process.** In this section, we present numerical simulation results to illustrate how the geometric parameters of the Miura origami sheet affect the dynamic deployment process. We specifically explore the influence of the sector angle $\gamma$ and the crease length ratio $\bar{b}$. The geometric parameters under investigation are varied while the other parameters remain at their nominal values. In the nominal pattern, the sector angle $\gamma = 60$ deg, crease length ratio $\bar{b} = 1$, and the number of units in the sheet is three. In this geometric parametric study, the stiffness parameters are ($\bar{r}_k = 100$, $\bar{k}_f/\bar{k}_{f0} = 1$) and the deployment control rate is set to be 0.6 [−/sec].

With the given stiffness parameters, the study in Sec. 3 showed that the structure would deploy with little deviation from the rigid kinematic configuration ($\bar{r}_k = 100$, $\bar{k}_f/\bar{k}_{f0} = 1$ in Fig. 6). By changing the geometric parameters, the effective stiffness will change, thus affecting the dynamic deployment behavior. In Fig. 13 we show the deviation of dynamic deployment of a three-unit Miura origami sheet with different sector angles and crease length ratios. We find that the peak nodal deviation $\delta$ increases with the increasing crease length ratio $\bar{b}$. This phenomenon can be explained by the increase of structural flexibility as reflected by the decreasing natural frequency shown in Fig. 10(*a*). By increasing the sector angle $\gamma$, the nodal deviations remain constant or increase slightly until they reach a boundary marked by a white dashed–dotted line in Fig. 13. To the left and above the boundary line, the nodal deviations are much higher than that to the lower right side on the contour plot, indicating a qualitative change in the deployment behavior. To gain more insight into this discontinuity, we first perform two case studies: in Sec. 4.3.1, we fix the crease length ratio at 1 and vary the sector angle (yellow line in Fig. 13), and in Sec. 4.3.2 we fix the sector angle at 60 deg and vary the crease length ratio (magenta line in Fig. 13). In Sec. 4.3.3, we further explore the geometric influence, and show that this discontinuity is due to a second stable equilibrium of the structure.

*4.3.1 Case study on the Sector Angle $\gamma$ When $\bar{b} = 1$.* In this section, we discuss the influence of the sector angle $\gamma$ on the deployment dynamics when the crease length ratio $\bar{b}$ is set to 1. Figure 13(*a*) shows that the nodal deviation $\delta$ slightly increases as the sector angle increases in the range of $\gamma \in [30\,\text{deg}, 59.4\,\text{deg}]$. A sharp decrease in nodal deviation occurs between $\gamma = 59.4$ deg and 59.6 deg, which corresponds to the intersection of the contours near the white curve in Fig. 13. This decrease occurs because the deployment process is qualitatively different between the structures with a sector angle of $\gamma < 59.4$ deg and those with $\gamma \geq 59.4$ deg (Fig. 14). During the deployment process, the structure with $\gamma = 59.4$ deg first snaps into a distorted configuration with a high deviation (Fig. 14(*c*)). As the structure deploys, it first becomes more distorted (Fig. 14(*d*)), and then, around the middle of the deployment process, it returns to a configuration that is near the rigid folded state. The structure then has little deviation until it becomes fully deployed (Fig. 14(*e*)). The structure with $\gamma = 59.6$ deg also deforms into a distorted configuration when it is first released (Fig. 14(*f*)), but quickly returns near to the rigid unfolding configuration (Fig. 14(*g*)) and maintains little deviation until

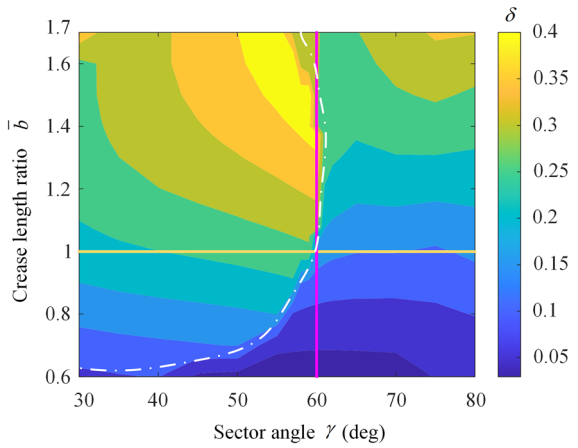


**Fig. 13 The nodal deviation of the dynamic deployment process of the Miura sheet structure with different geometric parameters. The sector angle $\gamma$ is varied with the *x*-axis and the crease length ratio $\bar{b}$ with the *y*-axis. The vertical line (magenta in colored version) shows the case when the crease length ratio is varied with a fixed sector angle at 60 deg; the horizontal line (yellow in colored version) represents the case when the sector angle is varied with a crease length ratio fixed at 1.**

fully deployed (Fig. 14(*h*)). This sharp drop in nodal deviation and the corresponding change in deployment behavior indicate that a slight change in sector angle can cause a qualitative change to the dynamic deployment process.

*4.3.2 Case Study on the Crease Length Ratio $\bar{b}$* When $\gamma = 60$ deg. In this section, we discuss the effect of the crease length ratio $\bar{b}$ on the dynamic deployment behaviors of the Miura origami sheet, when the sector angle $\gamma$ is kept at 60 deg. Results in Fig. 15(*a*) show that the nodal deviation $\delta$ increases and eventually approaches a constant value as the crease length ratio $\bar{b}$ increases. However, the curve shows a discontinuity in its middle part, which corresponds to the two intersections between the magenta line and the white curve in Fig. 13. The overall increase of $\delta$ with $\bar{b}$ is because the structure becomes wider and thus softer with higher $\bar{b}$, which is consistent with the results in Fig. 10(*a*). We then investigate the discontinuity in the relationship between $\delta$ and $\bar{b}$, which are the sudden increase of 41.5% in $\delta$ at $\bar{b} = [1.051, 1.052]$ and the drop of 23.1% at $\bar{b} = [1.375, 1.380]$. The deployment process is illustrated by the time history of deviation $\delta$ in Fig. 15(*b*). For $\bar{b} \in [1.052, 1.375]$, the structure will be in a distorted configuration (distorted from the rigid kinematic configuration) at the beginning of the deployment process (shown in Figs. 15(*b*), 15(*f*)–15(*g*), and 15(*i*) and 15(*j*)). This distortion will result in higher deviation $\delta$ than the structure with crease length ratio of $\bar{b} \in [0.6, 1.051] \cap [1.380, 1.7]$, in which the structure is mostly close to the rigid kinematic configuration during the deployment process (Figs. 15(*b*), 15(*c*)–15(*e*) and 15(*l*)–15(*n*)). The qualitative change in configuration indicates the existence of multiple equilibria of the Miura Origami sheet. The structure can approach different equilibrium configurations during deployment, depending on the shape of the origami pattern resulting in different levels of deviation from the rigid kinematic deployment path. The nodal deviation for different geometric patterns can differ by more than a factor of ten as shown in Fig. 15(*a*), which confirms the importance of the origami geometric effect on deployment dynamics.

*4.3.3 Localized Multistability During the Dynamic Deployment.* The dynamic analyses in Secs. 4.3.1 and 4.3.2 show significantly different deployment behaviors for origami sheets with different geometric designs. In this section, we will demonstrate that these deviations occur because the structure can snap between different stable states during the deployment process.

We start with a case study to investigate the structural multistability by analyzing the structure with a crease length ratio $\bar{b} = 1.2$ and a sector angle of $\gamma = 60$ deg where we observe the distinct increase in deviation as shown in Fig. 15(*a*). We use a quasi-static simulation to find stable equilibrium states of the structure and to verify that there do in fact exist multiple stable states. We use an iterative process on the static governing equations (delete the time varying terms and inertial/damping effects from the dynamic EOM), similar to Sec. 4.1, where the nodal positions of the origami are updated until we converge to a configuration that minimizes the sum of the internal forces in the structure. When we start the iterative process from the rigid folding configuration, we consistently converge to the first stable equilibrium state which has little deviation from the rigid folding orientation (dark blue images in Fig. 16). To search for a second stable equilibrium state, we need to begin the iterative process from another initial state where the structure is already deformed. We pick an initial deformed state corresponding to the shape of the origami during a transient dynamic deployment (magenta images in Fig. 16). With these initial conditions, the structure can converge to another

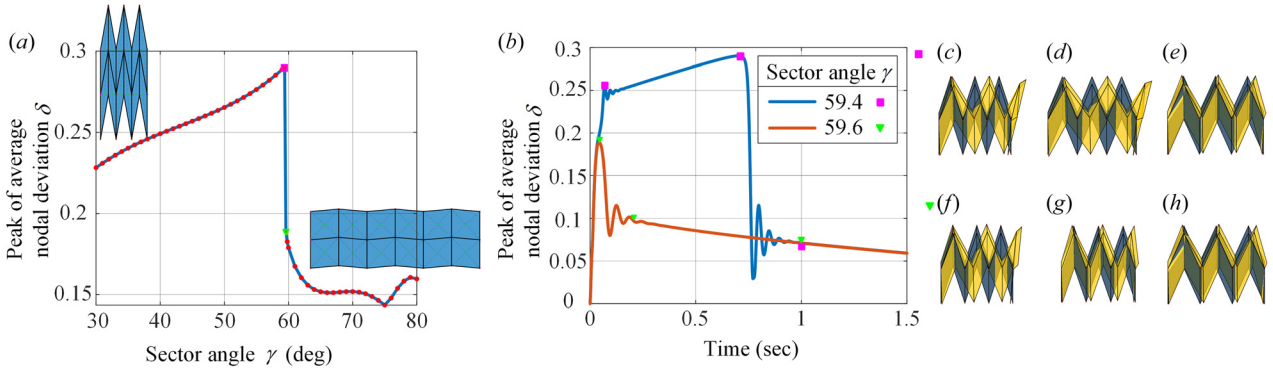


**Fig. 14 (*a*) Nodal deviation $\delta$ during the deployment process with respect to the sector angle (each dot represents the result of an individual deployment analysis). The two embedded images show the extreme values of sector angle $\gamma = 30$ deg and $\gamma = 80$ deg. (*b*) Time history of the nodal deviation for the structures with different sector angles. The lighter shade (yellow in colored version) refers to the dynamic deployment configuration, while the darker shade (blue in colored version) refers to the corresponding rigid unfolding configuration at the same stage of deployment. (*c*–*e*) are snapshots of the configuration during deployment for $\gamma = 59.4$ deg, in which (*c*) refers to 0.069 s, (*d*) to 0.709 s, and (*e*) to 1 s, corresponding to the squares (pink in colored version) on the curve (blue in colored version) in (*b*). (*f*–*h*) are snapshots of the configuration during deployment for $\gamma = 59.6$ deg, in which (*f*) refers to 0.044 s, (*g*) to 0.2 s, and (*h*) to 1 s, corresponding to the triangles (green in colored version) on the curve (red in colored version) in (*b*). The structures here have a crease length ratio of $\bar{b} = 1$.**

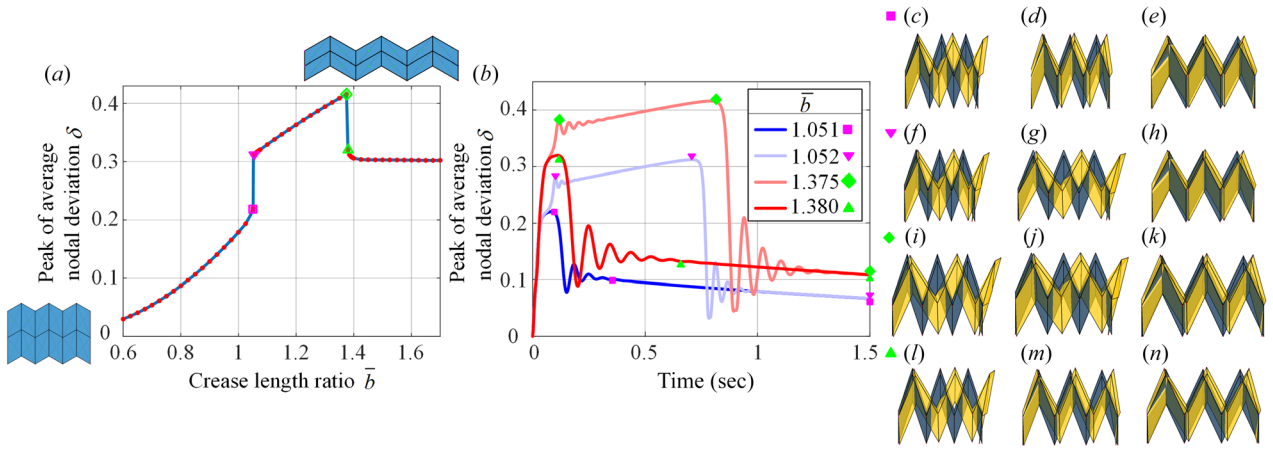


**Fig. 15 (*a*) Nodal deviation $\delta$ with respect to the crease length ratio $\bar{b}$ (each dot represents the result of an individual deployment analysis). (*b*) Time history of the nodal deviation for structures with crease length ratios of $\bar{b} = [1.051, 1.052, 1.375, 1.380]$. Snapshots of the sheet configuration during deployment, where the ligher shade (yellow in colored version) refers to the dynamic deployment configuration, and the darker shade (blue in colored version) refers to the corresponding rigid unfolding configuration at the same stage of deployment. (*c*)–(*e*) are for $\bar{b} = 1.051$ at (*c*) 0.082 s, (*d*) 0.35 s, and (*e*) 1.5 s, corresponding to the pink squares in (*b*). (*f*–*h*) are for $\bar{b} = 1.052$ at (*f*) 0.1 s, (*g*) 0.71 s, and (*h*) 1.5 s, pink triangles in (*b*). (*i*–*k*) are for $\bar{b} = 1.375$ at (*i*) 0.116 s, (*j*) 0.796 s, and (*k*) 1.5 s, green rhombi in (*b*). (*l*–*n*) are for $\bar{b} = 1.380$ at (*l*) 0.116 s, (*m*) 0.65 s, and (*n*) 1.5 s, green triangles in (*b*). The structures here have a sector angle of $\gamma = 60$ deg.**

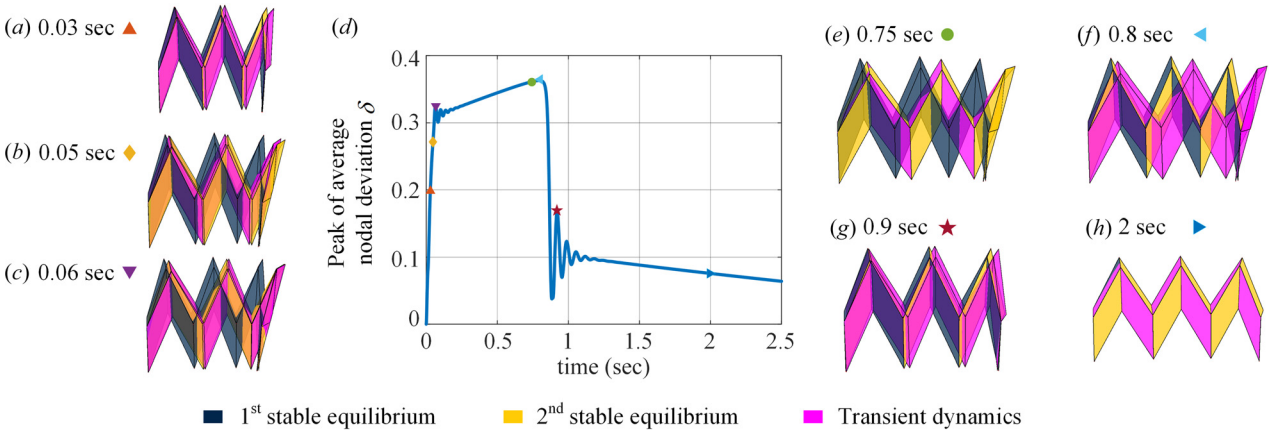


**Fig. 16 Stability analysis of a three-unit origami sheet with crease length ratio $\bar{b} = 1.2$ and sector angle $\gamma = 60$ deg. (*d*) Time history of nodal deviation $\delta$. (*a*–*c*, *e*–*h*) Configurations of the stable equilibria and snapshots of the transient dynamic deployment at selected deployment stages. The lightest (yellow in colored version) and darkest (blue in colored version) refer to the two stable equilibria, and the medium shade (magenta in colored version) refers to the snapshot in dynamic deployment. The stiffness parameters are ($\bar{r}_k = 100$, $\bar{k}_f/\bar{k}_{f0} = 10$).**

stable equilibrium (yellow images in Fig. 16), which is markedly different from the first (blue images), and has a substantial deviation. Figure 16 shows the two stable states of the origami sheet and the transient shape of the sheet at different stages of the deployment process. When the dynamic process begins. the structure snaps into the second stable equilibrium (0–0.06 s Figs. 16(*a*)–16(*c*)) where it has a large deviation from the rigid folded state (Fig. 16(*d*)). Furthermore, as the structure becomes more deployed this second equilibrium state deviates more from the rigid folded state (0.06–0.75 s Figs. 16(*c*) and 16(*e*)), which leads to a further increase in the nodal deviation (Fig. 16(*d*)). As the origami reaches a more deployed state (0.8 s Fig. 16(*f*)), we can no longer find the same second stable equilibrium, even when we start the iterative process with a deformed initial configuration. While other stable equilibria may exist, the nearest stable equilibrium is the same as the first, and thus the structure snaps back to the first stable equilibrium during the dynamic deployment (0.8–1.1 s Figs. 16(*f*)–16(*g*)). The dynamic deployment process experiences some transient oscillations after each time the structures snaps into a new configuration (∼0.06 s and ∼0.9 s in Fig. 16(*d*)). For higher states of deployment, the transient dynamics closely follow the first stable equilibrium (Fig. 16(*h*)).

We next extend this same multistability analysis to other origami sheets with different sector angles and crease length ratios. The yellow region in Fig. 17(*a*) shows the geometries where the structure snaps into and stays near the second stable equilibrium during the dynamic deployment process. The boundary of this region is also similar to the white curve in Fig. 13, to the left of which the structure undergoes higher nodal deviation. We find that during the dynamic deployment structures with some geometries (Figs. 17(*b*) and 17(*d*)) snap and oscillate near the second stable equilibrium, but structures with other geometries may not (Figs. 17(*c*) and 17(*e*)). The structure is still multistable to the right of the boundary (i.e., two stable equilibria can be found in Figs. 17(*c*) and 17(*e*)) but a snap does not occur during deployment. This different behavior is because the snap-through depends not only on the existence of multistability, but also other factors such as the initial strain energy that drives the deployment and the initial conditions of the system. Both quantities are well known to influence the response in nonlinear structural dynamics.

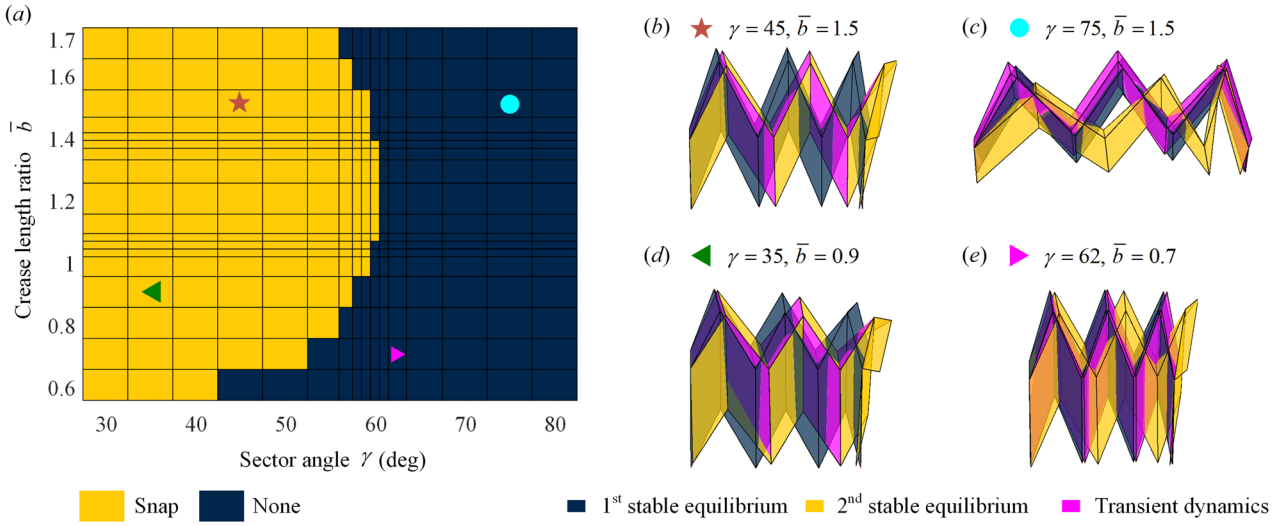


**Fig. 17 Dynamic behaviors and multistability of a three-unit origami sheet with different crease length ratios and sector angles. (*a*) The light (yellow in colored version) region represents the parameter sets with which the origami sheet snaps into and stays at the second stable equilibrium during the dynamic deployment process. (*b–e*) Configurations of the two stable equilibria, the darkest (blue in colored version) and the lightest (yellow in colored version), for selected pattern geometries. The medium shade (magentain colored version) shape is the deformed state of a snapshot from a transient deployment analysis that was used to find the second stable equilibrium. The stiffness parameters are ($\bar{r}_k = 100$, $\bar{k}_f/\bar{k}_{f0} = 10$).**

From this parametric study, it is shown that the geometry, including pattern shape and number of units in the sheet, can affect the structural effective stiffness and modal eigenvalues, indicating that the structure properties can be varied by designing the origami pattern. Numerical simulation further shows significantly different dynamic response of the Miura origami sheet with different geometries. Under the same displacement control, structures with certain geometric designs are shown to be able to follow the rigid kinematic path better, which is explained by the multistability analysis, indicating that the origami geometry can be designed for more desirable deployment behavior. These results will provide a foundation for the exploration and understanding of origami design for desired deployment performance.

## 5 Influence of Deployment Control Rate

Prior sections have illustrated how the stiffness and geometry of the structure affect the dynamic deployment process when the deployment rate is fixed to 0.6 [−/sec]. However, the deployment behavior also depends on how fast the structure is controlled to deploy. In our study, the structure is deployed while controlling the horizontal displacement at the right end with a constant velocity. Without loss of generality, we vary the deployment control rate from 0.05 [−/sec] to 1000 [−/sec]. To understand the influence of the deployment control rate, we perform analysis where we change the rate, and compute the average nodal deviations. In these studies, the nodal deviations are computed both with respect to the nominal rigid kinematic unfolding configuration, and with respect to a quasi-static deployment configuration (prediction considering the panel flexibility but not the inertial effect). The structure is a three-unit Miura origami sheet with geometric parameters ($\gamma = 60$deg, $\bar{b} = 1$). We perform this rate analysis on structures with different stiffness parameters ($\bar{r}_k$, $\bar{k}_f/\bar{k}_{f0}$) and present the results in Fig. 18.

**5.1 Comparison Between Dynamic Deployment and Rigid Kinematic Unfolding.** In this section, we derive the peak-averaged nodal deviation $\delta$ between the dynamic deployment process and the nominal rigid kinematic unfolding to explore the rate effect. In Fig. 18(*a*), under extremely low and high deployment control rates, the structure deviates from the rigid unfolding configuration the most. When deployed slowly, the units inside the Miura origami sheet experience nonuniform deformation where the left units are stretched, and the right unit is compressed. This deformation occurs especially at the beginning stage when the structure is near folded, and the strain energy is high (Figs. 19(*a*)–19(*c*)). As the deployment control rate is increased, the sheet deploys more uniformly and the deviation decreases. There exists a critical value $v_r$ for the control rate, where the structure experiences a minimum deviation. For the system with stiffness parameters of ($\bar{r}_k = 10$, $\bar{k}_f/\bar{k}_{f0} = 1$) the critical rate is $v_r = 17$[−/sec] with snapshots of the deployment process shown in Figs. 19(*e*)–19(*g*). If the deployment control rate continues to increase, then $\delta$ will increase again. At deployment rates that are much higher than $v_r$, the structure will be stretched during the deployment (Figs. 19(*j*)–19(*i*)), and after it reaches a fully deployed state. it will continue to undergo oscillations that deviate from the rigid unfolding path (Fig. 19(*k*)). This type of analysis can provide guidance for selecting a deployment control rate, which minimizes the deformation and deviation from the rigid kinematic deployment configuration.

The critical value of the deployment control rate $v_r$ under which the structure achieves minimum deviation is affected by the stiffness properties. Rate control analyses are performed for structures with different stiffness parameters, and the results are presented in Figs. 18(*c*) and 18(*d*). These results show a similar tendency as in Fig. 18(*a*) where $\delta$ will first decrease to a minimum deviation at a critical rate $v_r$, and then increase with the increase in deployment control rate. By comparing Fig. 18(*a*) with Fig. 18(*b*), and 18(*c*) with 18(*d*) where the stiffness ratios are kept constant ($\bar{r}_k = 10$ and $\bar{r}_k = 100$, respectively), but the fold stiffness $\bar{k}_f/\bar{k}_{f0}$ is increased, it can be seen that the structures with stiffer creases (b, and d) have a higher $v_r$ than those with softer creases (a and c). The higher $v_r$ is because structures with stiffer creases possess more strain energy and will undergo more nonuniform deformation induced by the higher strain energy. Thus, the structure needs to be deployed faster to avoid the nonuniform deformations. Additionally, by comparing Fig. 18(*a*) with 18(*b*) and 18(*b*) with 18(*d*) where the creases stiffness is kept constant ($\bar{k}_f = 3.8 \times 10^{-7}$ ($\bar{k}_f/\bar{k}_{f0} = 1$) and $\bar{k}_f = 3.8 \times 10^{-6}$ ($\bar{k}_f/\bar{k}_{f0} = 10$), respectively), but the stiffness ratio is increased, we can see that the structures with a higher ratio $\bar{r}_k$ have lower $v_r$. This lower deployment rate for the structures with a higher stiffness ratio is because their relatively stiffer panels can better restrain the squeezing deformations among units and thus the structure can be deployed at a lower rate. Additionally, the higher stiffness ratio $\bar{r}_k$ (closer to the rigid

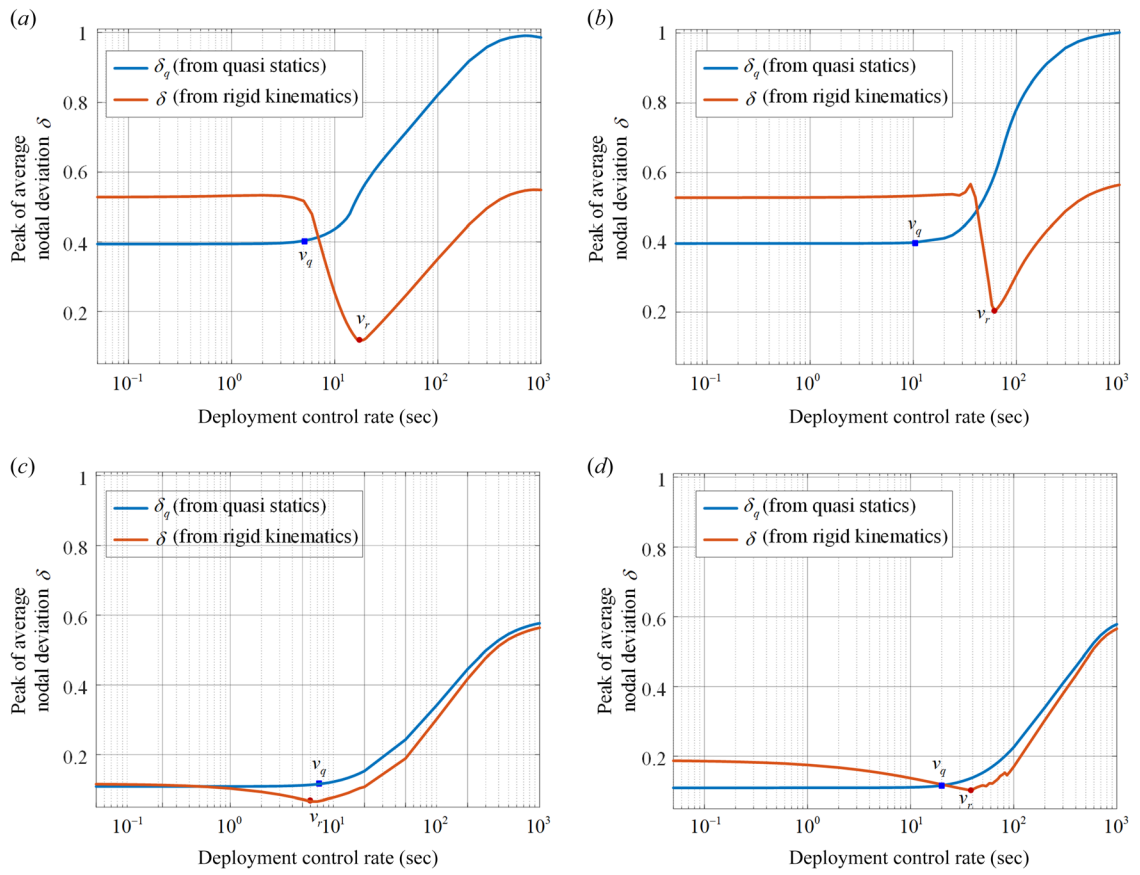


**Fig. 18 Nodal deviation with respect to the deployment control rate. A logarithmic scale is used for the deployment control rate in the *x* axis. The curve (red in colored version) with a round point shows the nodal deviation $\delta$ between the dynamic and rigid kinematic unfolding process. The curve (blue in colored version) with a square point shows the nodal deviation $\delta_q$ between the dynamic and quasi-static deployment The stiffness parameters are: (*a*) ($\bar{r}_k = 10$, $\bar{k}_f/\bar{k}_{f0} = 1$), (*b*) ($\bar{r}_k = 10$, $\bar{k}_f/\bar{k}_{f0} = 10$), (*c*) ($\bar{r}_k = 100$, $\bar{k}_f/\bar{k}_{f0} = 1$), and (*d*) ($\bar{r}_k = 100$, $\bar{k}_f/\bar{k}_{f0} = 10$).**

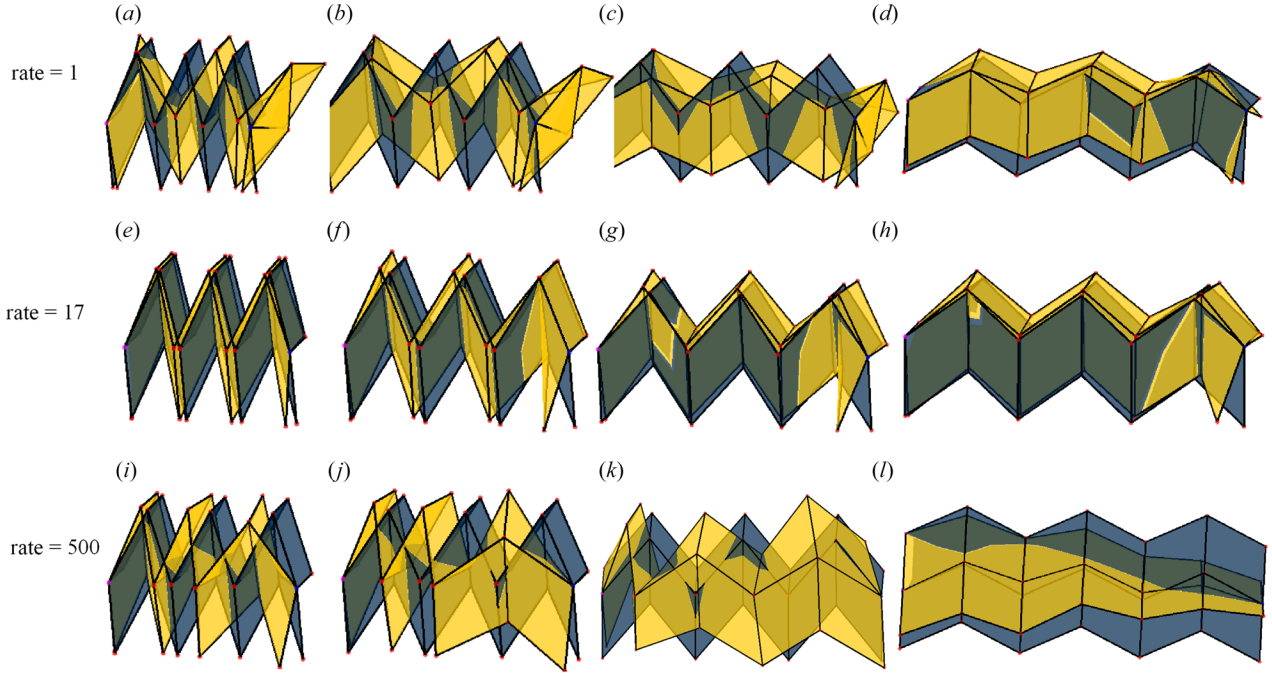


**Fig. 19 The deployment process of the structure with stiffness parameters ($\bar{r}_k = 10$, $\bar{k}_f/\bar{k}_{f0} = 1$) with the deployment control rate of (*a–d*) 1 [−/sec]; (*e–g*) 17 [−/sec]; and (*h–k*) 500 [−/sec]. The structure exhibits significantly different behaviors under the different deployment control rates. The light shade (yellow in colored version) refers to the dynamic deployment configuration, while the dark shade (blue in colored version) refers to the corresponding rigid unfolding configuration at the same stage of deployment: (*a*) $t = 0.1$ sec, (*b*) $t = 1$ sec, (*c*) $t = 2$ sec, (*d*) $t = 3$ sec, (*e*) $t = 0.01$ sec, (*f*) $t = 0.05$ sec, (*g*) $t = 0.1$ sec, (*h*) $t = 0.15$ sec, (*i*) $t = 0.001$ sec, (*j*) $t = 0.002$ sec, (*k*) $t = 0.004$ sec, and (*l*) $t = 0.009$ sec.**

kinematics unfolding scenario) results in an overall lower $\delta$ because there is less panel deformation and less deviation (i.e., similar to results from Sec. 3).

Under very fast deployment, there exists an upper limit on $\delta$. For the structure in Fig. 18(*a*) ($\bar{r}_k = 10,\ \bar{k}_f/\bar{k}_{f0} = 1$) we approach the upper limit with the deployment rate close to 1000 [−/sec]. For that case, the maximum deviation $\delta$ occurs at a time of 0.004 s during the deployment and the corresponding snapshot is shown in Fig. 19(*j*). The comparison between the snapshot of the dynamic deployment and the corresponding rigid configuration shows squeezing among the units, where the leftmost unit is compressed while the rightmost unit is stretched by the displacement control. The upper limit in deviation exists because of this large distortion between units. As the deployment control rate keeps increasing, the leftmost unit will become less compressed and the total $\delta$ will start decreasing slightly (Fig. 18(*a*)).

**5.2 More insight on the Role of Inertia and Flexibility in Dynamic Deployment.** The deviation of the origami dynamic deployment from the nominal rigid kinematic unfolding configuration originates from both the panel flexibility and the inertial effects. In this section, the dynamic deployment is compared with the quasi-static deployment process (which includes the panel flexibility but not the inertial effect) to understand more about the role of inertia. The nodal deviation between the dynamic and the quasi-static deployment configurations is denoted by $\delta_q$. At low deployment control rate, $\delta_q$ remains constant, meaning that the inertial effect on the dynamic deployment process does not change much with the rate. As the control rate exceeds a turning point $v_q$, shown as a blue square in Fig. 18, the nodal deviation $\delta_q$ increases corresponding to an increase of the inertial effects.

To gain more insight on the effects of the panel flexibility and system inertia, we compare the two types of deviation, $\delta$ and $\delta_q$. Both the effects of flexibility and inertia are reflected in $\delta$ while only the inertial effect is reflected in $\delta_q$. At low control rate, the cases with inertia have a larger deviation ($\delta > \delta_q$) because inertia dependent oscillations occur after the initial release of strain energy which drives the structure into a nonuniform squeezed shape (Fig. 19(*a*)). At higher control rates, $\delta < \delta_q$, due to the combined inertia and flexibility effects.

Additionally, the turning point changes with the stiffness of the structure. By comparing Fig. 18(*a*) with 18(*b*), as well as Fig. 18(*c*) with 18(*d*), the structure with stiffer folding creases ((*b*) and (*d*)) has a higher $v_q$, meaning that the quasi-static panel deformation dominates the overall nodal deviation for a wider range of deployment rates. On the other hand, the stiffness ratio $\bar{r}_k$ has relatively low influence on $v_q$, as can be seen by comparing Fig. 18(*a*) with 18(*c*), as well as Fig. 18(*b*) with 18(*d*).

## Conclusion

In this research, we investigate the dynamics of deployment of a Miura origami sheet. For the first time, through analyzing a novel dynamic model that includes the combination of panel inertia and flexibility, we uncover new phenomena and qualitative features that have not been observed previously and cannot be derived via traditional quasi-static and rigid kinematic unfolding analyses. Some of the system behaviors observed in the analysis are also shown experimentally on a test prototype. By analyzing the deviation of the dynamic deployment configurations from those of the traditional approaches, the tools we developed as well as the outcomes can provide quantitative information (e.g., parametric space) of where the deployment dynamics would become important for better system design and control.

We develop the dynamic model by considering panel inertia and flexibility, where we discretize the structure by using equivalent lump mass elements. We derive the nondimensionalized equations of motion and perform analysis to gain general understanding of the system dynamic behaviors during deployment. The deployment of the origami sheet is facilitated by the stored strain energy in the creases when the structure is folded and a displacement control on one end point of the sheet.

With different stiffness, the structure may exhibit qualitatively very different deployment behaviors. In cases where the fold stiffness to panel stiffness ratio ($\bar{r}_k$) is low, the structure may undergo a large global bending "pop-up" state. This pop-up occurs at different stages depending on the stiffness ratio $\bar{r}_k$. As $\bar{r}_k$ becomes sufficiently large, the dynamic deployment would be closer to the rigid kinematic unfolding configuration without pop-ups. Specifically, there exists a critical value $\bar{r}_{km}$, below which the structure would undergo large pop-up motion. Such $\bar{r}_{km}$ value can vary with the number of units in the origami sheet, and in particular the $\bar{r}_k$ value needs to be higher for origami sheets with more units to avoid pop-up.

It is shown that apart from the material stiffness parameters, the pattern geometry including the crease length ratio and the sector angle can influence the structural effective stiffness properties, and thus affect the transient dynamics of the deployment process. It is discovered that the origami sheet possesses multiple stable equilibria under different geometric parameters and may reconfigure between the stable equilibria during dynamic deployment.

We found that the dynamic deployment performance can also be affected by changing the control deployment rate. Under slow rates, the origami sheet undergoes squeezing among its units, while it undergoes stretching under fast rates. The structure can best follow the rigid kinematic configuration under a certain value of the control rate, which also varies with the structure properties, such as fold stiffness. These results indicate that the displacement control can be utilized to obtain more desirable dynamic deployment performance.

Overall, this research provides a foundation for the exploration and understanding of the dynamic characteristics of origami sheet deployment. The tools and insights developed can be utilized to design for desired (e.g., smooth and fast) deployment or intentional reconfiguration of origami sheet structures. Moreover, they are especially valuable in raising awareness of new phenomena that have not been observed in the past, and providing original guidelines to create origamis with design parameters (e.g., material and geometric properties) and operating conditions (e.g., deployment rate) that are outside the traditional range of consideration. In other words, this basic research is impactful in extending our fundamental knowledge and expanding our comfort zone with the deployment dynamics of origami.


## Acknowledgment

The authors are grateful to Janice Tardiff and Chaitanya Nimmagadda from the Ford Motor Company, for many helpful discussions regarding this work. The authors are grateful for the support from Yi Zhu on the prototype design and experimental setup.

## Funding Data

- Ford-University of Michigan Alliance Framework (Funder ID: 10.13039/100002427).
- National Science Foundation (NSF) (Grant No. CMMI #1634545; Funder ID: 10.13039/100002427).
- NSF Grant CAREER (Grant No. 1943723; Funder ID: 10.13039/100000147).


## References


[1] Schenk, M., Viquerat, A. D., Seffen, K. A., and Guest, S. D., 2014, "Review of Inflatable Booms for Deployable Space Structures: Packing and Rigidization," J. Spacecr. Rockets, **51**(3), pp. 762–778.

[2] Shah, S. H., and Lim, S., 2017, "Transformation From a Single Antenna to a Series Array Using Push/Pull Origami," J. Sens., **17**(9), p. 1968.

[3] Ahmed, S., Kamel, A., and Mahmoud, W., 2020, "Methodology for Using Origami in Designing Deployable Shelters," J. Des. Sci. Appl. Arts, **1**(2), pp. 20–37.

[4] Miyashita, S., Guitron, S., Li, S., and Rus, D., 2017, "Robotic Metamorphosis by Origami Exoskeletons," Sci. Robot., **2**(10), p. eaao4369.
[5] Gabler, F., Karnaushenko, D. D., Karnaushenko, D., and Schmidt, O. G., 2019, "Magnetic Origami Creates High Performance Micro Devices," Nat. Commun., **10**(1), p. 3013.
[6] Zhu, Y., Birla, M., Oldham, K. R., and Filipov, E. T., 2020, "Elastically and Plastically Foldable Electrothermal Micro-Origami for Controllable and Rapid Shape Morphing," Adv. Funct. Mater., **30**(40), p. 2003741.
[7] Miura, K., 1985, "Method of Packaging and Deployment of Large Membranes in Space," Inst. Sp. Astronaut. Sci. Rep, **618**, pp. 1–9.
[8] Callens, S. P., and Zadpoor, A. A., 2018, "From Flat Sheets to Curved Geometries: Origami and Kirigami Approaches," Mater. Today, **21**(3), pp. 241–264.
[9] Lebée, A., 2015, "From Folds to Structures, a Review," Int. J. Sp. Struct., **30**(2), pp. 55–74.
[10] Tachi, T., 2010, "Origamizing Polyhedral Surfaces," IEEE Trans. Vis. Comput. Graph, **16**(2), pp. 298–311.
[11] Liu, X., Gattas, J. M., and Chen, Y., 2016, "One-DOF Superimposed Rigid Origami With Multiple States," Sci. Rep., **6**, pp. 1–9.
[12] Li, S., Fang, H., Sadeghi, S., Bhovad, P., and Wang, K. W., 2019, "Architected Origami Materials: How Folding Creates Sophisticated Mechanical Properties," Adv. Mater., **31**(5), p. 1805282.
[13] Overvelde, J., de Jong, T., Shevchenko, Y., Becerra, S. A., Whitesides, G. M., Weaver, J. C., Hoberman, C., and Bertoldi, K. A., 2016, "Three-Dimensional Actuated Origami-Inspired Transformable Metamaterial With Multiple Degrees of Freedom," Nat. Commun., **7**, p. 10929.
[14] Li, S., and Wang, K. W., 2015, "Fluidic Origami: A Plant-Inspired Adaptive Structure With Shape Morphing and Stiffness Tuning," Smart Mater. Struct., **24**(10), p. 105031.
[15] Fang, H., Li, S., Ji, H., and Wang, K. W., 2016, "Uncovering the Deformation Mechanisms of Origami Metamaterials by Introducing Generic Degree-Four Vertices," Phys. Rev. E, **94**(4), pp. 1–11.
[16] Fang, H., Li, S., and Wang, K. W., 2016, "Self-Locking Degree-4 Vertex Origami Structures," Proc. R. Soc. A Math. Phys. Eng. Sci., **472**(2195), p. 20160682.
[17] Filipov, E. T., Tachi, T., Paulino, G. H., and Weitz, D. A., 2015, "Origami Tubes Assembled Into Stiff, Yet Reconfigurable Structures and Metamaterials," Proc. Natl. Acad. Sci. U. S. A., **112**(40), pp. 12321–12326.
[18] Li, S., and Wang, K. W., 2015, "Fluidic Origami With Embedded Pressure Dependent Multi-Stability: A Plant Inspired Innovation," J. R. Soc. Interface, **12**(111), p. 20150639.
[19] Li, S., Fang, H., and Wang, K. W., 2016, "Recoverable and Programmable Collapse From Folding Pressurized Origami Cellular Solids," Phys. Rev. Lett., **117**(11), pp. 1–5.
[20] Ma, J., Song, J., and Chen, Y., 2018, "An Origami-Inspired Structure With Graded Stiffness," Int. J. Mech. Sci., **136**, pp. 134–142.
[21] Waitukaitis, S., Menaut, R., Chen, B. G., and van Hecke, M., 2015, "Origami Multistability: From Single Vertices to Metasheets," Phys. Rev. Lett., **114**(5), p. 055503.
[22] Fang, H., Wang, K. W., and Li, S., 2017, "Asymmetric Energy Barrier and Static Mechanical Diode Effect From Folding," Ext. Mech. Lett, **17**, pp. 7–15.
[23] Sengupta, S., and Li, S., 2018, "Harnessing the Anisotropic Multi-Stability of Stacked-Origami Mechanical Metamaterials for Elastic Modulus Programming," J. Intell. Mater. Syst. Struct, **29**(14), pp. 2933–2945.
[24] Hanna, B. H., Lund, J. M., Lang, R. J., Magleby, S. P., and Howell, L., 2014, "Waterbomb Base: A Symmetric Single-Vertex Bistable Origami Mechanism," Smart Mater. Struct., **23**(9), p. 094009.
[25] Thota, M., and Wang, K. W., 2017, "Reconfigurable Origami Sonic Barriers With Tunable Bandgaps for Traffic Noise Mitigation," J. Appl. Phys, **122**(15), p. 154901.
[26] Thota, M., Li, S., and Wang, K. W., 2017, "Lattice Reconfiguration and Phononic Band-Gap Adaptation Via Origami Folding," Phys. Rev. B, **95**(6), pp. 1–10.
[27] Yasuda, H., Chong, C., Charalampidis, E. G., Kevrekidis, P. G., and Yang, J., 2016, "Formation of Rarefaction Waves in Origami-Based Metamaterials," Phys. Rev. E, **93**(4), pp. 1–11.
[28] Liu, S., Lu, G., Chen, Y., and Leong, Y. W., 2015, "Deformation of the Miura-Ori Patterned Sheet," Int. J. Mech. Sci., **99**, pp. 130–142.
[29] Fathers, R. K., Gattas, J. M., and You, Z., 2015, "Quasi-Static Crushing of Egg-box, Cube, and Modified Cube Foldcore Sandwich Structures," Int. J. Mech. Sci., **101–102**, pp. 421–428.
[30] Gattas, J. M., and You, Z., 2014, "Quasi-Static Impact of Indented Foldcores," Int. J. Impact Eng., **73**, pp. 15–29.
[31] Fang, H., Li, S., Ji, H., and Wang, K. W., 2017, "Dynamics of a Bistable Miura-Origami Structure," Phys. Rev. E, **95**(5), pp. 27–29.
[32] Ishida, S., Uchida, H., Shimosaka, H., and Hagiwara, I., 2017, "Design and Numerical Analysis of Vibration Isolators With Quasi-Zero-Stiffness Characteristics Using Bistable Foldable Structures," ASME J. Vib. Acoust. Trans. ASME, **139**(3), p. 031015.
[33] Ishida, S., Suzuki, K., and Shimosaka, H., 2017, "Design and Experimental Analysis of Origami-Inspired Vibration Isolator With Quasi-Zero-Stiffness Characteristic," ASME J. Vib. Acoust, **139**(5), p. 051004.
[34] Sadeghi, S., and Li, S., 2019, "Fluidic Origami Cellular Structure With Asymmetric Quasi-Zero Stiffness for Low-Frequency Vibration Isolation," Smart Mater. Struct., **28**(6), p. 065006.
[35] Bhuiyan, H., and Emran, M., 2017, "Dynamic Modeling and Analysis of Strain Energy Deployment of an Origami Flasher," Electronic thesis or dissertation, University of Toledo, OhioLINK Electronic Theses and Dissertations Center.
[36] Kidambi, N., and Wang, K. W., 2020, "Dynamics of Kresling Origami Deployment," Phys. Rev. E, **101**(6), p. 63003.
[37] Wu, H., Fang, H., Chen, L., and Xu, J., 2020, "Transient Dynamics of a Miura-Origami Tube During Free Deployment," Phys. Rev. Appl., **14**(3), p. 034068.
[38] Miura, K., 2009, "The Science of Miura-Ori," Origami, **4**, pp. 87–99.
[39] Li, M., Shen, L., Jing, L., Xu, S., Zheng, B., Lin, X., Yang, Y., Wang, Z., and Chen, H., 2019, "Origami Metawall: Mechanically Controlled Absorption and Deflection of Light," Adv. Sci., **6**(23), p. 1901434.
[40] Gattas, J. M., and You, Z., 2014, "Miura-Base Rigid Origami: Parametrizations of Curved-Crease Geometries," ASME J. Mech. Des., **136**(12), pp. 1–10.
[41] Wu, S. R., Chen, T. H., and Tsai, H. Y., 2019, "A Review of Actuation Force in Origami Applications," J. Mech., **35**(5), pp. 627–639.
[42] Peraza-Hernandez, E. A., Hartl, D. J., and Lagoudas, D. C., 2019, Active Origami.
[43] Peraza-Hernandez, E. A., Hartl, D. J., Malak, R. J., and Lagoudas, D. C., 2014, "Origami-Inspired Active Structures: A Synthesis and Review," Smart Mater. Struct., **23**(9), p. 094001.
[44] Martinez, R. V., Fish, C. R., Chen, X., and Whitesides, G. M., 2012, "Elastomeric Origami: Programmable Paper-Elastomer Composites as Pneumatic Actuators," Adv. Funct. Mater., **22**(7), pp. 1376–1384.
[45] Zirbel, S., Trease, B., Magleby, S., and Howell, L., 2014, "Deployment Methods for an Origami-Inspired Rigid-Foldable Array," Proceedings of the 40th Aerospace Mechanisms Symposium NASA Godda, Baltimore, MD, pp. 189–194.
[46] Liu, K., and Paulino, G. H., "MERLIN: A MATLAB Implementation to Capture Highly Nonlinear Behavior of Non-Rigid Origami," Proceedings of IASS Annual Symposia, IASS 2016 Tokyo Symposium: Spatial Structures in the 21st Century, Origami, Tokyo, Japan, pp. 1–10.
[47] Liu, K., and Paulino, G. H., 2018, "Highly Efficient Nonlinear Structural Analysis of Origami Assemblages Using the MERLIN2 Software," Merlin2, Origami, 7(4), pp. 1167–1182.
[48] Filipov, E. T., Liu, K., Tachi, T., Schenk, M., and Paulino, G. H., 2017, "Bar and Hinge Models for Scalable Analysis of Origami," Int. J. Solids Struct., **124**, pp. 26–45.
[49] Liu, K., and Paulino, G. H., 2017, "Nonlinear Mechanics of Non-Rigid Origami: An Efficient Computational Approach†," Proc. R. Soc. A., **473**(2206), p. 20170348.
[50] Filipov, E. T., Paulino, G. H., and Tachi, T., 2016, "Origami Tubes With Reconfigurable Polygonal Cross-Sections," Proc. R. Soc. A, **472**(2185), p. 20150607.